Doctoral Dissertation

Application of CMOS-based Devices for Dual-site Fluorescent Imaging of Pain Processing Brain Regions

痛み関連神経ネットワーク回路解明に向けた CMOS 蛍光イメージングデバイスのマウス脳内複数同時埋植に関する研究

Romeo Brioso Rebusi, Jr.

March 2022

Nara Institute of Science and Technology

Division of Materials Science

Application of CMOS-based Devices for Dual-site Fluorescent Imaging of Pain Processing Brain Regions

Romeo Brioso Rebusi, Jr.

Photonic Device Science Laboratory

Division of Materials Science

Nara Institute of Science and Technology

Supervisor

Professor Jun Ohta

ABSTRACT

The use of various imaging implantable devices and their accompanying set-ups has given much progress in various neurological studies. With the visualization of neuronal activity, specifically calcium signaling, expressed as fluorescence in GFP transgenic mice, activation of many brain regions during behavior is brought to light. The methods of inner-brain imaging involving implants, or endoscopy, are of various types, depending on the mechanisms involved for image acquisition and the consequent quality of the data provided. Most of the methods involve the use of an implanted refractive component for use with microscopes, which can be tabletop or miniaturized, to be mounted on free-moving and conscious experimental animals. This system provides high-resolution data that can discriminate among individual neurons. Though it can yield high-quality output, the head-mounted equipment is bulky and heavy and can hinder animal behavior and prevent multiple brain-site recordings at once.

My work throughout the doctoral program has been for the development and the demonstration, in the context of pain processing, of the applications of an innovative implantable needle-type imaging device developed by our lab. The device is very lightweight and does not involve any lenses or microscopy. Instead, the imaging component is CMOS-based. The well-miniaturized features of the device, when compared to other endoscopes, provide a much smaller burden on moving, active experimental animals and permit the visualization of more than one brain area at a time. It allows for angled implantation paths to avoid critical areas of the brain.

The set-up of the imaging system consists of a data-collecting desktop PC connected to a double-board module developed by our lab. The imaging devices are connected to this module, via a cable, and also to power sources, one per device board. Image data acquisition is by the use of the dedicated CIS-NAIST program, also developed by our lab. The needle-type device has been structurally modified for greater implantation accuracy.

Improvements have been implemented into the surgical method for implanting the devices. They ensure the welfare of the experimental mice is maintained and also to minimize errors that will prevent the successful imaging of the very small brain region targets. Because of the refinement of the equipment features and the implantation procedure, the targeting accuracy for the specific brain sites has improved at every experimental trial, though complications still remain.

To demonstrate the use of the device in actual in vivo experiments involving animals and to further its development, the formalin test was done. This test is a standard method for inducing and observing pain through the subcutaneous injection of low-concentration formaldehyde on a hind paw of a rodent, and in my work's case, the left hind paw of GCaMP6 transgenic mice. I have done this test on double-implanted mice and collected fluorescence neuron activity data during the experience of pain, nociception. The target brain regions were the central amygdala (CeLC) and the dorsal raphe nucleus (DRN) of the right hemisphere, both involved in pain processing in various degrees. To confirm the presence of pain in mice, visual behavior data, specifically the licking of the injected hind paw, were also collected. Overall, the collected data showed that inner-brain fluorescence increase is correlated with

nociception. The timing of the fluorescence also matched with the expected bi-phasic pain response of the formalin test.

To further test the utility of the devices, double-implanted mice were used in a modified formalin test. The brain region targets were the same as before. In this phase, the formalin test was combined with the von Frey tactile test to observe signs of hyperalgesia or pain-induced tactile hypersensitivity. Von Frey filaments of varying hardness were used to stimulate touch on the injected hind paws of formalin- and saline-injected mice to determine if formalin-derived inflammatory pain led to tactile hypersensitivity. As baseline, some mice were subjected to the formalin test using the same set-up, but did not receive tactile stimulation. Neuronal activity fluorescence has shown differences in activity among the groups. Fluorescence intensity was linked to the presence or absence of hyperalgesia in mice.

Overall, the results I had collected across my doctoral course have demonstrated that the devices can be used successfully to collect viable data from pain experiments. With the improvements in the various aspects of the device utilization methodology, implantation accuracy and animal welfare were made more possible. This body of work can be used as the basis for further improvement, development, and expansion on how the needle-type fluorescence-imaging implantable devices can be applied to other methodologies.

Dedication

I would like to dedicate this thesis and all the effort it represents to all the animals used and will use in my work. The improvements I've done on the scientific method have been very much for the consideration of their welfare. May their sacrifice not be wasted and lead towards the greater good.

Acknowledgements

I would like to express truly my deepest gratitude to all those who helped me reach this point and allow me to present to you this thesis.

Professor Jun Ohta

My panel members: Professor Yukiharu Uraoka and Professor Hironari Kamikubo

Associate Professor Kiyotaka Sasagawa

Associate Professor Hiroyuki Tashiro

Assistant Professor Makito Haruta

Assistant Professor Hironari Takehara

Dr. Yasumi Ohta

Ms. Mamiko Kawahara

Ms. Juri Hotta

Ms. Ryoko Fukuzawa

The staff of the International Affairs Office

The staff of the MS Office

Mark Christian Guinto and Joshua Philippe Oloricisimo

The Filipino Community, and those who have left

Associate Professor Masahiro Ohsawa of NCU

Professor Takashi Tokuda

Assistant Professor Satoko Maki

Professor Sonia Jacinto of UPD

Disclaimers

All animal handling procedures and experimentation were approved by the Nara Institute of Science and Technology (NAIST) Animal Committees, and were performed in accordance with the institutional guidelines of the animal facilities of NAIST.

Table of Contents

Abstract I

Dedication IV

Acknowledgements V

Disclaimers VI

Table of Contents VII

1. **Background of Work** 1

    a. Endoscopy for detection of fluorescent neuronal signals 1

    b. The CMOS-based fluorescence endoscope 3

    c. Pain-processing neural circuitry and experimentation 6

    d. Objectives 7

2. **The Double-board CMOS-imaging device System** 9

    a. Equipment assemblage 9

    b. Modifications to the equipment 14

3. **Animal Handling and the Implantation Method** 19

    a. Considerations on double-implantation 19

    b. The stereotaxic methodology 23

4. **Application on the Standard Formalin Test** 28

a. Methodology 28

b. Results 36

c. Discussion 49

d. Summary 56

5. **Application on the Modified von Frey – Formalin Test** 58

a. Methodology 58

b. Results 61

c. Discussion 66

d. Summary 67

6. **Conclusion** 68

a. Overview 68

b. Future direction and possible applications 70

7. **Bibliography** 73

8. **Appendix** 84

1. Background of Work

a. Endoscopy for detection of fluorescent neuronal signals

Calcium imaging is a well-established method that has allowed very precise imaging of neuron firing in real time (Grienberger and Konnerth, 2012). The basis of this method is the transient influx of ions, including calcium, during neuronal firing and the subsequent binding of said ions to various proteins as part of the activation pathway. In genetically modified or transgenic organisms, expression of certain proteins can allow the visualization of this calcium influx. Transgenic GCaMP animals express a modified green fluorescent protein (GFP) molecule within select cells that when bound to calcium, via a calmodulin conjugate, will change its configuration to allow for light-based excitation (~480 nm emission optimum) and a resulting fluorescence (~510 nm detection optimum). Theoretically, the amount inflowing calcium ions, and it follows also the collective neuronal activity, is linearly correlated to the intensity of the fluorescence. In actuality, optical properties of tissues and the variability of GFP expression in a single transgenic organism makes this correlation an incomplete, but still very reliable, representation of the actual neuronal activity and firing.

Fluorescence-imaging brain implants that can visualize calcium imaging have been indispensable to the field of neurobiology. Their use has given much insight of the inner workings of the brain in vivo (Grienberger and Konnerth, 2012). There are a number of types of such devices than can be safely used in living animals without compromising the process of a study. Though all types have their advantages, they also

have limitations that must be acknowledged when considering their use. Selecting the appropriate tool can mean the success or failure of doing a study.

Microendoscopes have been used in fluorescence imaging of deep brain tissue. They come in multiple configurations, of differing materials and collection methods (Helmchen et al., 2001; Silva, 2017; Ozbay et al., 2018; Scott et al., 2018; Klioutchnikov et al., 2020). Resolution of collected images is enhanced by the inclusion of a focusing element or lens. The lens itself can be the endoscope, such as the gradient refraction index (GRIN lens). The available endoscopes can be rigid, such as the GRIN lens or silica-containing fibers, but have been miniaturized enough to be of practical use (Levene et al., 2004; Flusberg et al., 2005). These properties provide minimal invasiveness, but also limit mobility since use of these tools require restrained animals. Movement is necessarily restricted because of the fixed sizeable tabletop equipment required for the excitation light source and fluorescence emission collection.

Miniature head-mountable integrated microscopes, or miniscopes, are an innovation on the use of microendoscopes (Ziv and Ghosh, 2015; Resendez et al., 2016; Liberti et al., 2017; Jacob et al., 2018).They can be used to acquire high resolution images of brain activity from freely-moving animals. The implanted component is a cylindrical lens (e.g. GRIN lens) that refracts light to the microscope module secured on an animal's cranium. Though miniaturized, the sheer bulk needed to accommodate the components gives the device some weight, more than 2 grams in some cases (Helmchen et al., 2001; Ozbay et al., 2018; Scott et al., 2018; Klioutchnikov et al., 2020). This entails consideration for the weight burden on smaller experimental animals, such as mice, and the possible effects on brain activity (Ziv and Ghosh, 2015).

b. The CMOS-based fluorescence endoscope

An implantable brain activity-visualizing device consisting of a CMOS-based imaging component at the tip has been referred to either as “chip-on-tip” (Gorissen et al., 2018) or “camera-on-a-chip” (Friedman et al., 2015). The- two studies from where the terms were sourced used flexible endoscopes equipped with small CMOS imaging chips at the insertion ends to visualize the interior of the brain. Though of a similar fundamental concept, our lab has taken a different approach in the implementation. Instead, we emphasized rigidity and miniaturization of the implant and the enhancement of the fluorescence detection of the imaging component to better detect neuronal activity expressed as calcium-signaling fluorescence in unrestrained and conscious animals. This kind of CMOS-imaging implant can be applied to the detection of other inner-brain signals such as positron markers (Ammour et al., 2019).

Our lab has developed a needle-type implantable device that has the advantages of the aforementioned devices (**Fig. 1A**) (Ohta et al., 2017; Rustami et al., 2020; Sunaga et al., 2020). Our device uses a complementary metal-oxide semiconductor (CMOS)-based image sensor chip (imaging area of 120 by 40 pixels, 7.5 μm per pixel, hence 300 x 9000 μm) and a blue-light micro-LED (for green fluorescent protein (GFP) excitation), mounted on a thickened flexible printed-circuit substrate (FPC). It has a width of 0.7 mm, a thickness of 0.2 mm, an insertion allowance of up to 4.5 mm, and an average weight of 26.6 mg. Its small features and rigidity prevent excessive tissue damage, allow simultaneous implantation of another device, and make possible angled implantations to avoid critical areas and reach difficult sites. These manners of implantations are almost not applicable to the other types of imaging devices, especially

the head-mounted miniscopes, mostly due to their bulk. Their head-mounted modules will require additional support if oriented non-orthogonally. Though simultaneous use is still possible with the use of miniature microscopes (de Groot et al., 2020), our devices are much lighter, providing less of a burden on the test animal. The sensor chip allows for imaging of calcium signaling fluorescence, but not to the same resolution as microscopy imaging.

When implanted, the device is affixed in the braincase by dental cement applied on the skull and further anchored by screws also inserted directly on the skull. With this configuration, the imaging chip is held constant to a target brain region where it can image fluorescence of GFP-expressing cells up to 100μm from the imaging area surface (detection limit). Beyond this limit, regions of interest (ROIs) will not be reliably distinguished. (Takehara et al., 2016) (**Fig 1B**).

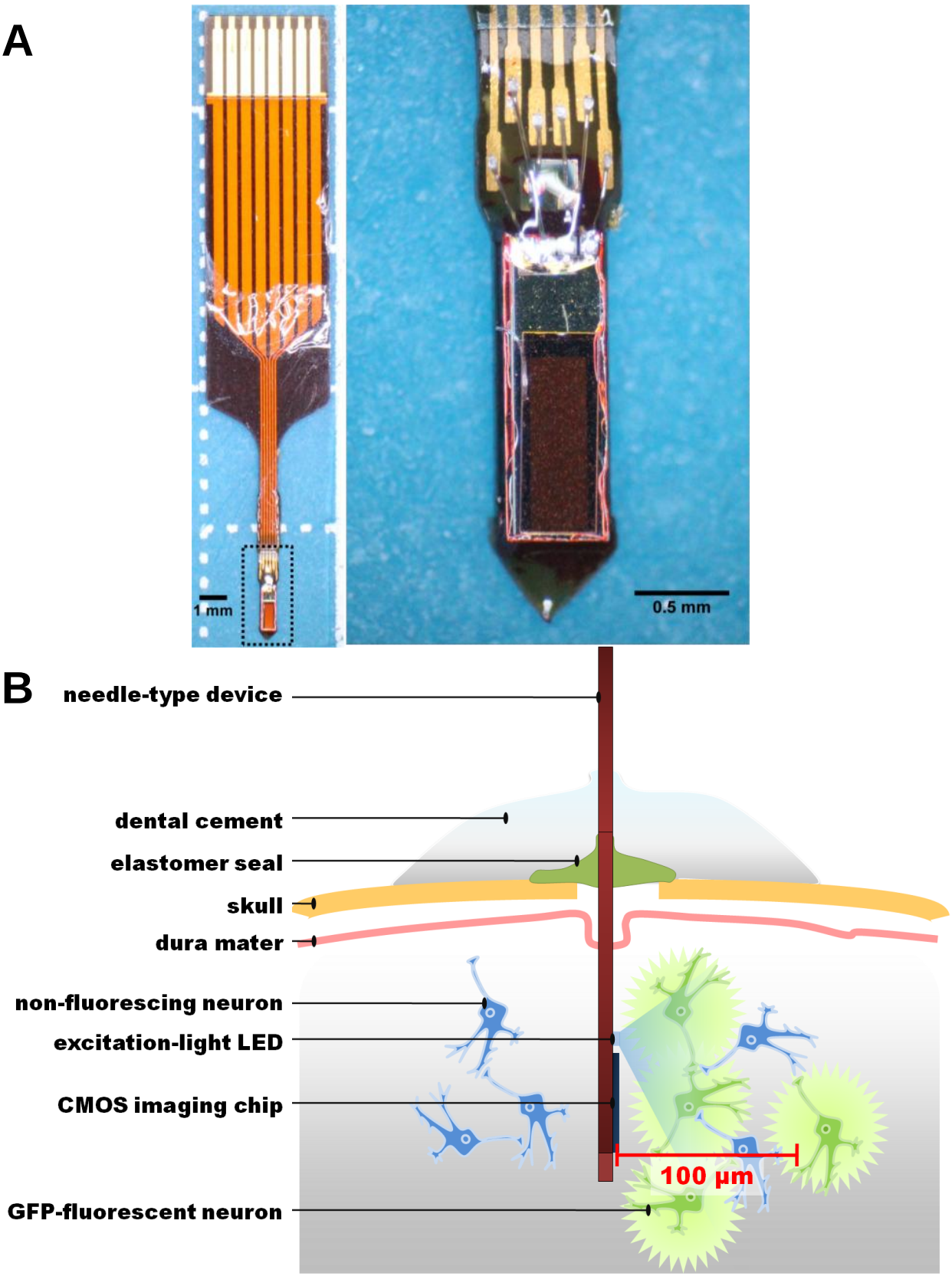
A
1 mm
0.5 mm
B
needle-type device
dental cement
elastomer seal
skull
dura mater
non-fluorescing neuron
excitation-light LED
CMOS imaging chip
GFP-fluorescent neuron
100 µm

Figure 1. CMOS-based implantable needle-type device for fluorescence imaging.(A) Left: Image of the needle-type implantable device as seen under a microscope (28x magnification). This device has undergone all steps of the fabrication process; Right: Higher magnification of the imaging device (from selection, 45x). (B) Diagram of the implanted needle-type imaging device and its immediate vicinity. The span colored red represents the detection limit of the CMOS imaging chip for calcium-signal GFP fluorescence in the brain. Note that not all neurons will sufficiently express the GFP molecule needed for fluorescence.

c. Pain-processing neural circuitry and experimentation

In my work, two of these implantable CMOS-based imaging devices were simultaneously used in mice induced to experience pain via subcutaneous formalin injection. Pain is an immediate and powerful aversive event that has prominent related behavior and can usually activate relevant brain sites with very low latency (review (Woolf, 2010)). In this way, pain stimulation gave rise to an immediate fluorescence signal that was easily attributed to the processing of the stimulus. This observed causation was further supported by cross-referencing with time-matched pain-related behavior, included in the data gathering.

The devices were to be implanted adjacent to the capsular-lateral subsection of the central amygdala (CeLC) and the dorsal raphe nucleus (DRN). The two brain regions are connected together via a serotonergic pathway arising from the DRN (Peyron et al., 1997; Garcia-Garcia and Soiza-Reilly, 2019). These two were selected

for imaging because of their variable roles in pain processing and related functions. Because of the more prominent and central role the CeLC has in pain processing, it has been expected that it will provide more intense calcium imaging signals. Such kind of data will have served as a benchmark for comparison to other weaker signals, such as what was expected from the DRN. Also, their relative locations had been considered as most sufficiently spaced apart for simultaneously implanted devices, especially in small animals such as mice.

The central amygdala has been regarded as a center of the processing of pain signals (Bernard et al., 1989; Neugebauer et al., 2004; Ossipov et al., 2010; Veinante et al., 2013) and responsible for pain-related behavior as an output center of the amygdala (Ji et al., 2017). Meanwhile, the DRN has been implicated in the process of pain modulation (Wang and Nakai, 1994; Stamford, 1995; Li et al., 2017; Lopez-Alvarez et al., 2018). Together, they are part of a system responsible for processing aversive stimuli and stress (Spannuth et al., 2011; Groessl et al., 2018; Ren et al., 2018; Garcia-Garcia and Soiza-Reilly, 2019; Zhou et al., 2019).

d. Objectives

My collective work has aimed to demonstrate two major points. First, it is to demonstrate that the simultaneous use of two devices on an unrestrained animal is feasible in an actual experimental setting. It would be with minimal physiological risk and also allows for unhindered behavior. Second, is to provide useful inner-brain imaging data of the pain processing circuitry. This is accomplished through calcium

imaging at the relevant sites during the experience of pain. The visual data must be able to be correlated with other indicators of nociception such as behavior or altered stimulus thresholds. Overall, I aim to showcase CMOS-imaging device features that can complement established brain imaging devices while also providing unique advantages. If I am to be successful in achieving said objectives, the improvement of the device can progress further and new methodologies in brain-activity visualization can be made possible, contributing to the development of neuroscience, especially in pain studies.

2. The Double-board CMOS-imaging device System

a. Equipment assemblage

The implanted imaging devices are connected to a series of equipment that facilitates data collection, power supply, and freedom of movement (**Fig.2A**).

The devices are immediately connected to lightweight relay cables via clamps (Fig 4.5). The other ends of these cables are connected to a slip ring that can accommodate two devices and allows for turning to prevent entanglement whenever the mouse spins. The slip ring allots electricity and allows for data collection via its connections to the LED power sources (6146 DC Voltage Current Source, ADCMT) and the double boards, respectively, one of each per device. These boards have been developed by our lab for the specific use with the CMOS-based imaging implants. They are housed in a single casing where they are provided electricity by power supplies (PK-80L, Matsusada Precision Inc.). These boards relay data signals via cables connected to specially fabricated cards that interface with the motherboard of a recording PC.

The recording personal computer (Windows 7 OS), with the CIS_NAIST program installed is the ultimate destination of the fluorescence visual data from the devices. This version of the program was developed to collect and display imaging data from two devices at the same time. The program can process visual data via a designated (or “grabbed”) reference image frame and present it in real time. This processing allows for better images by giving more visual detail. Adjustments can be made to fine tune parameters to enhance fluorescence signals and to visualize them in pseudocolor for better interpretation of fluorescence intensity (**Fig. 2B**)

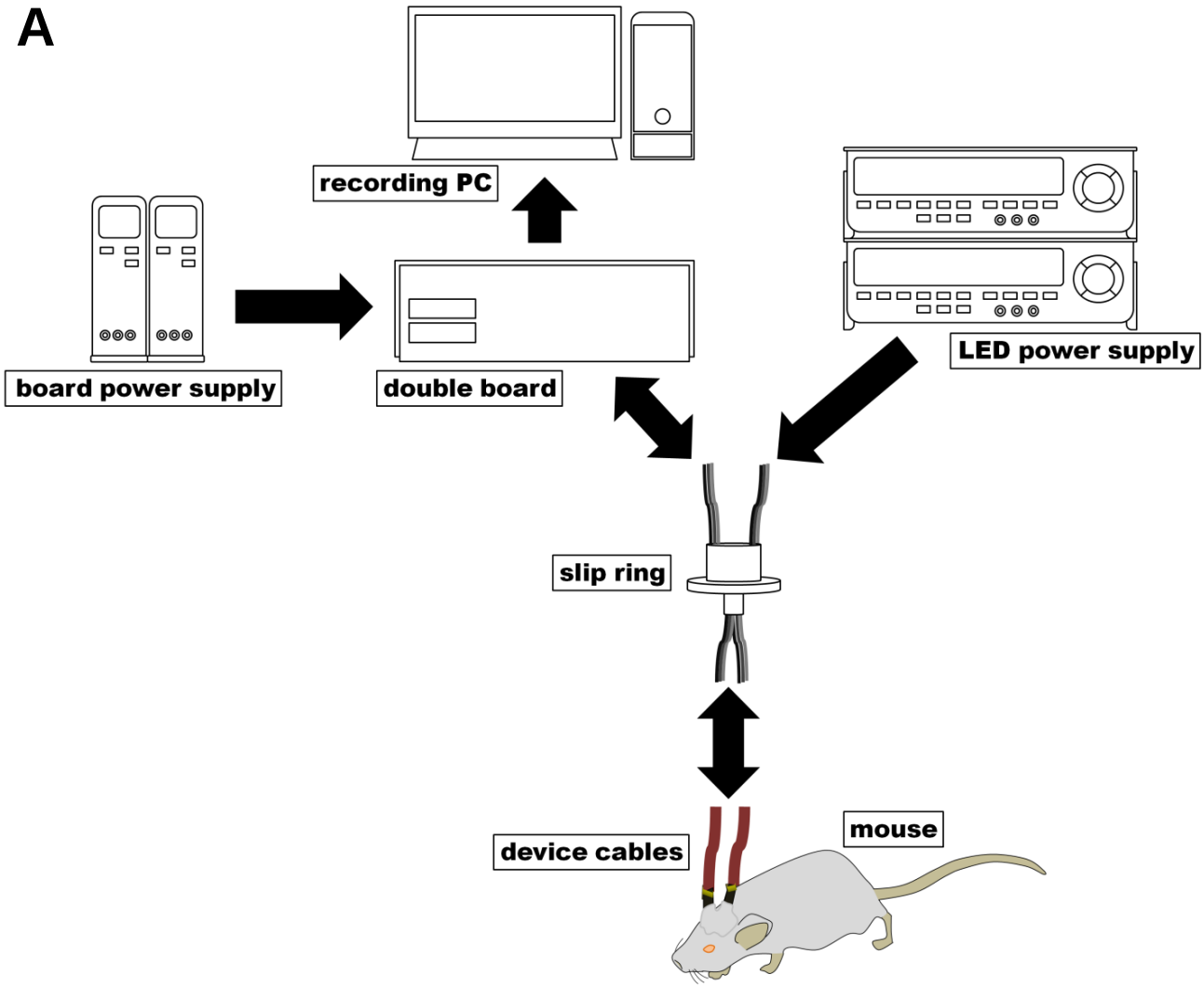
A
recording PC
board power supply
double board
LED power supply
slip ring
device cables
mouse

B

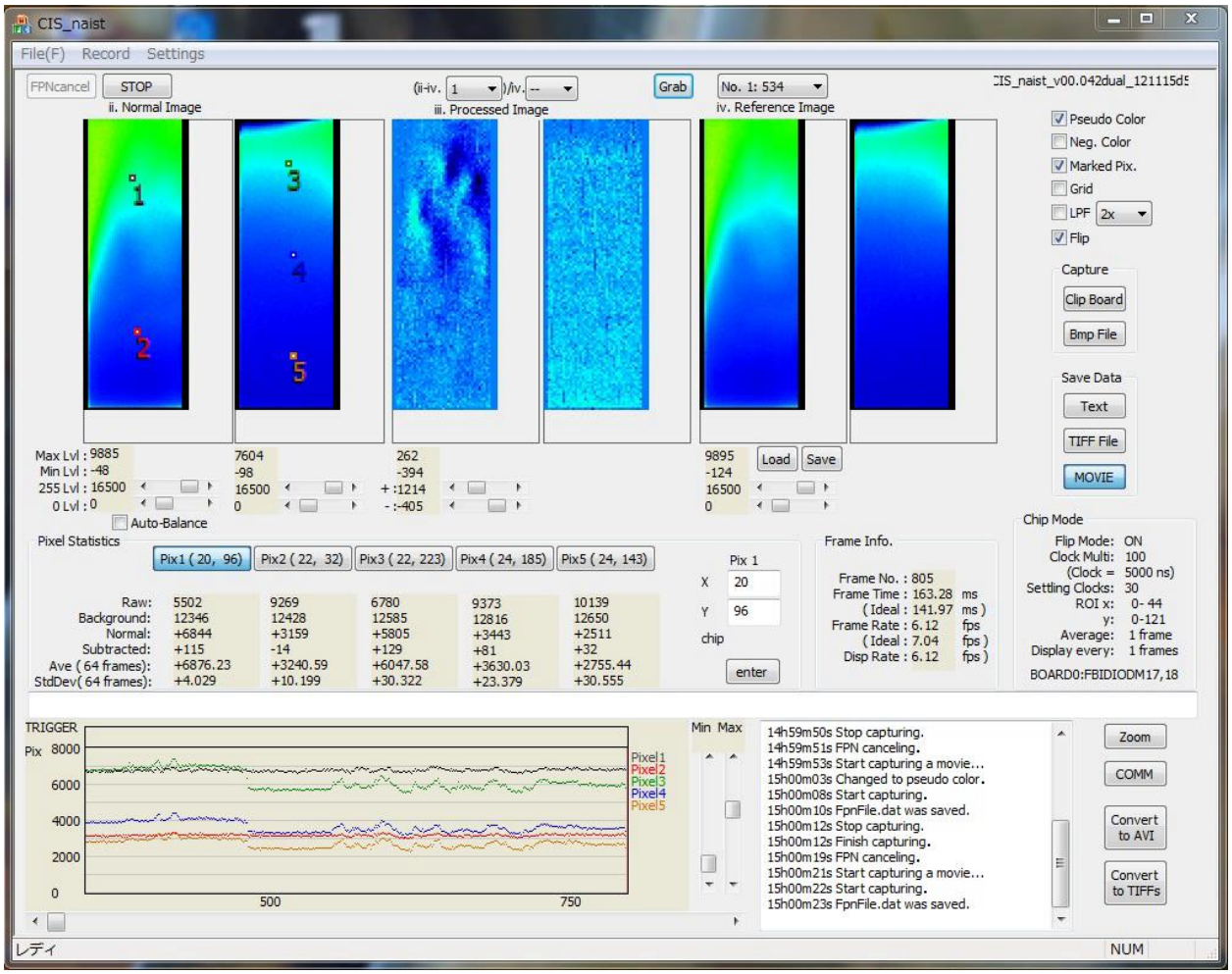

Figure 2. Image data collection module and power sources equipment for the double-board system (A) A schematic of the equipment that comprises the double-board system for the simultaneous recording of brain calcium signaling fluorescence of two sites; arrow directions indicate flow of power and data among the equipment. (B) The CIS_NAIST program as viewed in a computer monitor; data is presented in pseudocolor.

All imaging devices are fabricated by hand, so a great deal of mastery was needed for successful manufacture, especially for high-quality and resilient ones. The following will recount the fabrication process step by step.

The CMOS imaging chips, designed by our laboratory (**Fig. 3**), were cleaned by submersion in acetone (Fujifilm Wako), twice, and then in isopropanol (Fujifilm Wako) for 5 minutes each. After drying, they were each mounted on a polyimide, gold-circuit-printed FPC substrate (Taiyo Industrial) taped on a glass slide using a thin layer of epoxy resin (low viscosity epoxy resin Z-1 (N), CraftResin). The blue-light-emitting micro LEDs (ES-VEBCM12A, Epistar), with a central emission wavelength of 470 nm, were also mounted in the same fashion.

The blue-light filter was prepared by first dissolving Valifast Yellow 3150 dye (Orient Chemical Industries) with cyclopentanol (1:1, w/w) overnight in a light-proof vial. In the same container, the mixture was mixed with Norland Optical Adhesive 43 (Norland Products) (2:1, w/w) using a vortex. The resulting adhesive mixture was spin coated (Spincoater model: 1H-D7, Mikasa) on a silicon-coated (CAT-RG catalyst and KE-106 silicone (Shin-Etsu Chemical), 1:10, w/w) cover slipwith a size of 23mm x 23 mm under the following setting: 3 sec to 500 rpm – 5 sec at 500 rpm – 5 sec to 2000 rpm – 20 sec at 2000 rpm – 5 sec to 0 rpm. The spin coated material was immediately heated on a hot plate at 100°C for 30 minutes then left to set in room temperature overnight. The filter film was cut with an Nd: YAG laser (Callisto VL-C30RS-GV, TNS Systems) to make a grid of 10000x3500 μm sheets.

The cut filter sheet was manually placed over the entire imaging area of the CMOS chips. The device was baked in a vacuum oven (AVO-250NS, ETTAS) for 2 hours at 120°C and left to cool.

Using a needle, red resist resin (ST-3000L, Fujifilm) was applied on the sides of the CMOS chip. This resin prevented entry of stray blue LED light through the sides of the chip.

The CMOS chip and the LED were connected to the circuitry of the FPC with micro aluminum wires (Tanaka Electronics) using a wire bonder (7400C-79, West Bond). The wiring was sealed by a protective cover of epoxy resin (low viscosity epoxy resin Z-1 (N), CraftResin) and left to set overnight.

The processed device was incised off from the excess FPC material with a blade. The sides at the implantable end of the cut FPC substrate of the device were coated with a thin layer epoxy (low viscosity epoxy resin Z-1 (N), CraftResin) to cover jagged edges.

The devices were lined and bound together with a ribbon of Kapton tape and were enclosed in a parylene coater (PDS 2010, Specialty Coating Systems). They were coated with 5 grams of bio-protective dichloro-c-cyclophane (GalentisS.r.l.). The thickness of the parylene deposition layer is about 2.5 μm.

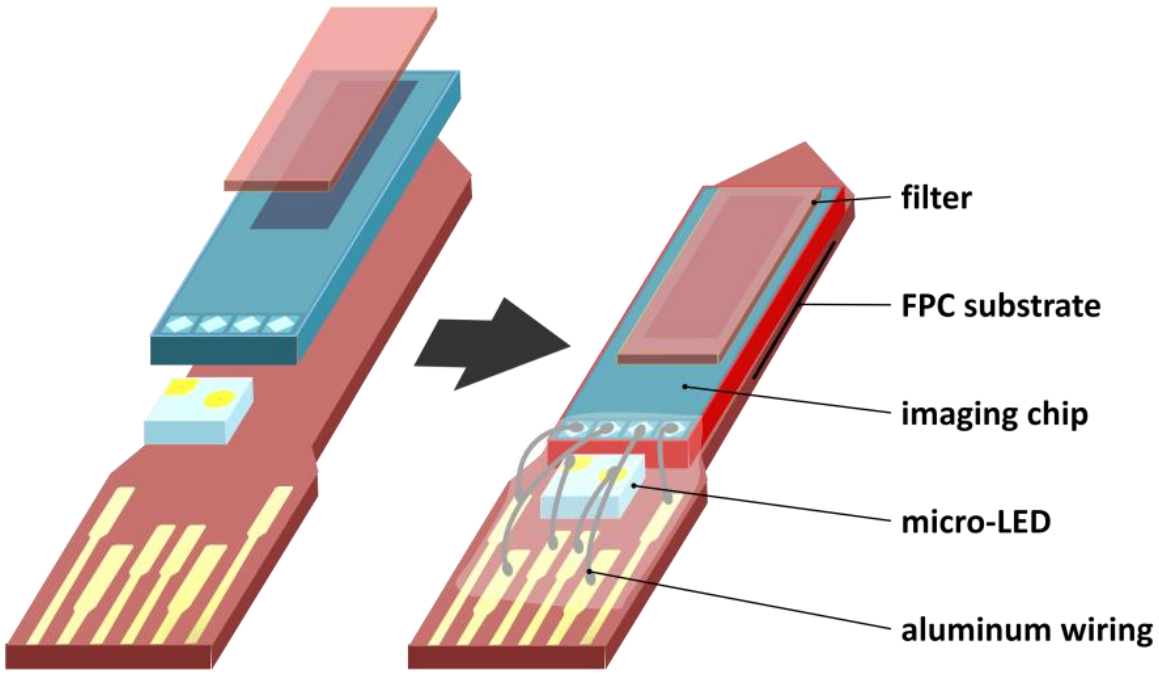

Figure 3. The needle-type imaging device and its components Partial breakdown of the device (left), and the placement of its components (right).

b. Modifications to the equipment

The brain targets of concern for the studies are very small, especially so for mice, with the CeLC measuring at ~1 mm and the DRN at ~1.5 mm long (along the antero-posterior axis) (Franklin and Paxinos, 2019). Thus, it is very important to optimize equipment and methodology to ensure the exact facing of the imaging area of the devices to the targets. This is also important because there is no feasible and practical way to actually ensure successful targeting during surgery. Also, since animals with mistaken targeting are removed from the data pool, it also important to be always accurate in the implantation to prevent wastage of lives and resources.

One of the advantages of the needle-type device is that it is very thin, reducing injury and burden on the experimental mice and making it easier to use. Unfortunately, such feature also allows it to be easily distorted, particularly during the process of the insertion into the brain. Though brain matter is very soft, jelly-like in consistency, the device is still too pliable to avoid warping when moving through the layers of the brain, especially its covering, the meninges. To address this problem, I provided some input as to reinforce the device structurally while retaining its miniscule dimensions to an acceptable degree.

The needle-type device was modified to make it more rigid to help it retain it shape when encountering resistance during implantation (**Fig 4**). In the initial base version, the wider portion of the FPC is thicker because it has a reinforcing plate layer compared to the insertion end, where the imaging and illumination components are. In the first modification version, the numbers of layers between both segments were matched. Though it had proved structurally more stable during use, it was deemed too thick, especially when used with another device with the same modification. In the second modification version, the reinforcing plate of the insertion end was removed making it less thick, but still more robust than the basal version. This configuration demonstrated sufficient rigidity, albeit reduced from the previous version, when used during implantation. Both versions of the device permitted better accuracy in reaching the target brain sites, though not perfectly since the slight curvature of the devices cannot fully be prevented. With everything considered, I settled for the second version of the modified FPC for use for all the experimental animals in work.

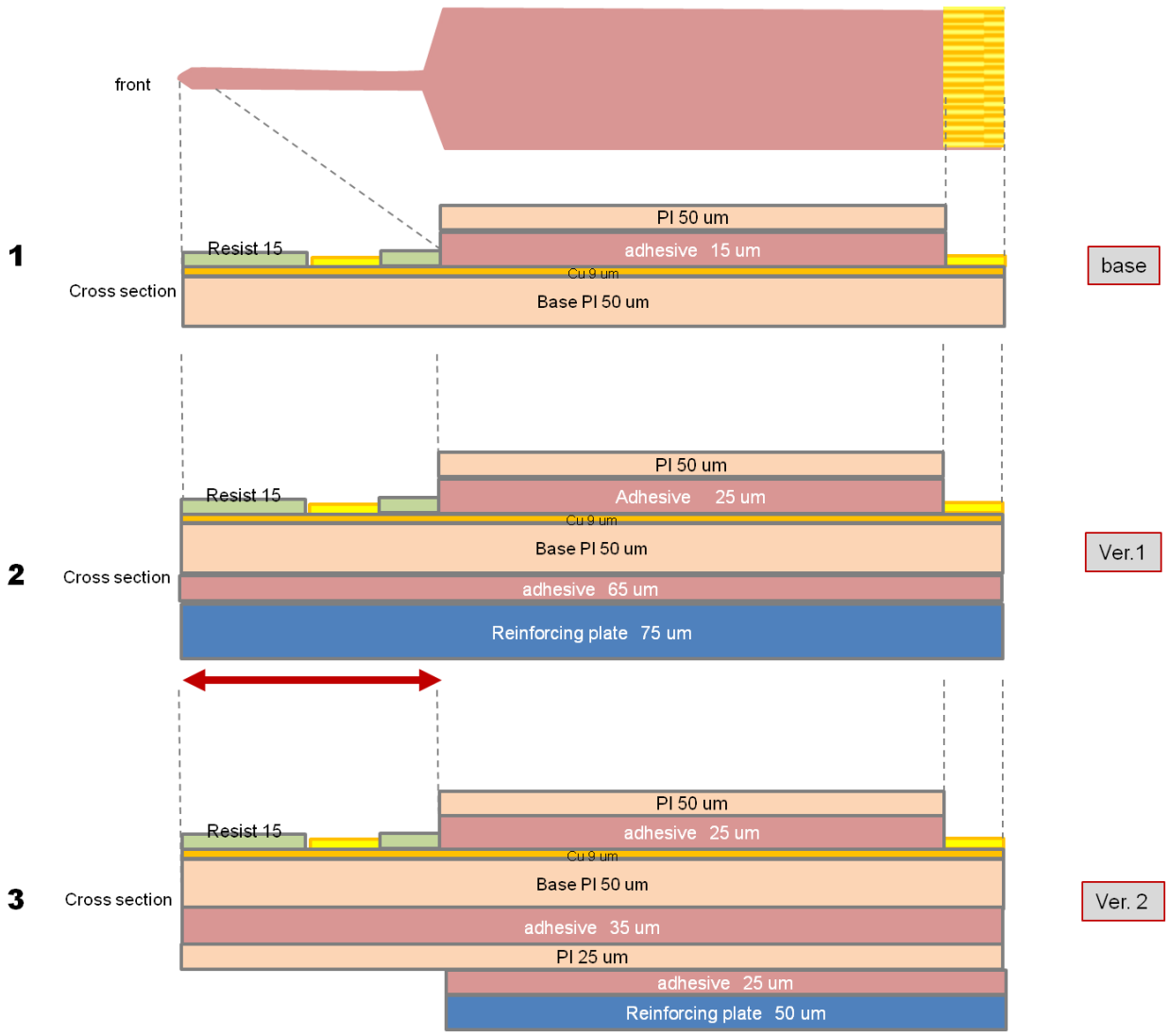

Figure 4. Modifications to the needle-type device FPC Schematics of the layering of the FPC structures across the various versions of the basal and the modified FPCs; lengths of the segments depicted in the cross sections are not to scale and are just for representation purposes

Another innovative feature of the needle-type devices is the relatively very low weight when compared to other endoscopy set-ups, providing a much smaller burden

on the implanted animal. Though, as with other inner-brain imaging methods involving implants, the actual weight burden include the other components immediately connected to the device that relay data and provide power.

In our device, the additional weight is significantly provided by the cable that connects it to the slip ring, which in turn is connected to the power supply and the recording equipment. To minimize burden, I modified the cable features to remove or replace components to lessen the weight while ensuring it is durable enough for use in active animals. The kind of wire used for a previous version of the cable was changed from a bundle of six thin PTFE wire (Junkosha Inc.) to a single Type 1 Litz wire (New England Wire Technologies) which is actually a bundle of small uninsulated wires, but of almost the same diameter as a single of the latter. Though the component wires are much thinner, it still provided sufficient and consistent connection while still being structurally sound. The new wire bundle had a much thinner covering making it not as rigid, so additional protective and lightweight covering was provided. This came in the form of segmented Kapton tape-scales, and later, a thin wrapping of Parafilm M (PM-996, Pechiney Plastic Packaging) (**Fig 5**).The reinforcement at the cable end where the device clamp is located was also changed from layers of heat-wrapped RSFR-H tubing and electrical tape to a coating of hot glue. Altogether, the modifications reduced the weight of the cable, even for a bit, which was more impactful when multiple are used at the same time. Ultimately, the Parafilm-covered wire was chosen to be used for most of the experiments because of its much lighter device-connection end (0.44 vs 0.63 g).

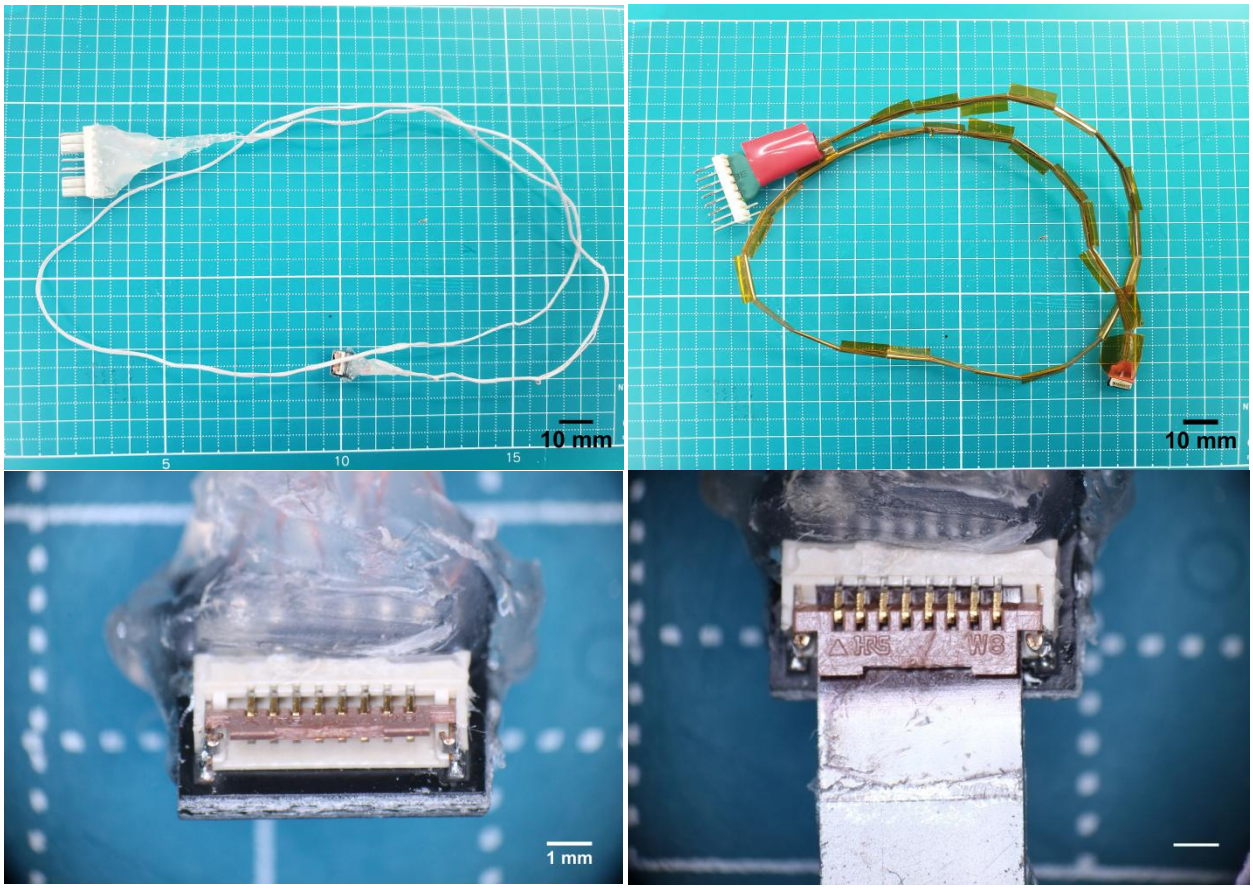

Figure 5. Modifications to the connecting cables for the implantable devices Various cable designs and their device clamps. Left images: Parafilm-wrapped wire with connection points reinforced with glue. Upper right image: Kapton tape-scale-covered wire with connection points reinforced with tubing and electrical tape. Lower right image: wire clamp clasped to a needle-type device.

3. Animal Handling and the Implantation Method

a. Considerations on double-implantation

The targets of my work are two brain regions involved in pain processing: the DRN and the CeLC. These regions are very small, so a high degree of implantation accuracy is required to successfully allow the imaging area of the implanted device to face the targets. Even small misalignments from the ideal implantation path, in terms of micrometers, can lead to failure in the very small mouse brain.

All coordinates for the brain region targets were initially derived from the Paxinos mouse brain map (Franklin and Paxinos, 2019). The coordinate values are the distances in millimetres from the starting points, namely the bregma, the anterior (front) intersection of four skull plates, and the mid-dorsal skull suture, the middle intersection of the side skull plates. These values are the front-back (antero-posterior, from the bregma) and lateral (medio-lateral, from the mid-dorsal line) distances and depth of implantation (dorso-ventral, from the surface of the brain).

The coordinates are most applicable for mice with an average weight of 28g. Because the size of the brain follows the weight of the mouse, the pre-determined coordinates might not be appropriate with those far from the average.

There is also the issue of some slight incompatibility of using the coordinates from the reference with stereotaxic devices, equipment used to hold animals during surgical implantation, of differing settings or calibration. The equipment used by the reference authors to find the brain region coordinates might be different enough to what

is available in our facilities. Using the same coordinates with various kinds of equipment, be it by brand or versions, will most likely lead to significant deviation, which is unacceptable when very high accuracy is required.

To address the issues with the mouse size variations and the differing equipment settings, implantation trials were done to determine the actual coordinates of the CeLC and the DRN. It was expected that the results from these trials would greatly reduce, and not fully remove, the differences between the expected and the actual location of the brain regions. All trials were done using wild-type (non-GMO) mice of various sizes, dummy needle-type devices, and the stereotaxic equipment that were to be used for the implantation of all experimental animals. When determining the coordinates, the optimal location and orientation of the CMOS chip imaging area was taken into account. So, the implantation path was set to be immediately adjacent to the imaging targets and not through them. The sectioning of the implanted brains and microscopy determined the success of the implantation. The schematics and images in the Paxinos brain map were used for cross-reference.

The derived coordinates were only applicable to the specific stereotaxic equipment used to locate them, so using another set-up will require another round of trials. They were also most appropriate to the size range of experimental mice, from 20 to around 25 g, with very slight approximated adjustments depending on the size.

As set by the guidelines on the use of the Paxinos brain map, for every implantation procedure, the points of intersection of the mouse brain sutures, the bregma and the more posterior lambda, were to be absolutely horizontally aligned to

ensure accuracy in targeting. The alignment was measured using a modified sterotaxic manipulator, with its tip fitted with a metallic implement that touches the brain surface to determine the height as read on the measure along the manipulator's side. The tilt of the mouse's snout was adjusted accordingly for the levelling.

Along with accuracy, minimization of damage of vital organs and structures near the site of implantation is also to be prioritized. This is to prevent any confounding factors from affecting the pain experiment procedure and also to ensure the welfare and survival of the animals. Any excessive injury arising from the implantation can compromise the results and will lead to the rejection of collected data from the affected animals, thus wasting their lives. The implantation path should be very carefully considered to avoid brain regions important to physiological functions, larger ventricles, and major blood vessels. One of the innovative features of the needle-type device is the ability to implant it an angled manner, giving more options for optimizing of the implantation path in terms of safety.

In the targeting of the DRN, the implantation path is tilted or angled 25° posteriorly to avoid an overlying major blood vessel located in between cerebellum and the posterior margin of the cerebrum (Xiong et al., 2017). This manner of implantation also prevents the clashing with the device for the DRN during surgery and experimentation. The angled implantation path was derived using basic trigonometry, with the original non-angled implantation depth as the triangle base. From there, the posterior displacement (triangle height) for device insertion and the new, angled implantation depth (hypotenuse) were calculated.

Though, blood loss during surgery is unavoidable, avoidance of major blood vessels can minimize it. In the case that excessive blood loss do occur during the preparation of the brain for implantation, the blood was continuously washed away with phosphate buffer saline (PBS) and wicked with sterile wipes until the bleeding subsided. Allowing blood to remain during the implantation of the devices can lead to the covering of the imaging area and the intrusion of blood deep into the brain which can lead to complications, such as brain hemorrhage.

The medio-lateral stereotaxic coordinates for both brain regions were also carefully considered and adjusted to mostly avoid two large ventricles, part of the "sewage system" of the brain: the lateral ventricles and the aqueduct (Franklin and Paxinos, 2008). Inclusions into the ventricles, mostly by blood in the case of implantation, might lead to the widespread brain inflammation. So, it would be better for the overall brain health of the implanted mice to leave the ventricles intact as much as possible.

The double implantation surgery requires more time and steps than a regular procedure. The longer the surgery takes place, with the interior of the head left exposed, the more the health of the mouse will be compromised. Also, more tasks during surgery lend to more chances for error. It was very important to standardize and optimize the workflow and always maintain the equipment in perfect working condition to ensure that the procedure was done as fast and properly as possible. Along with that, more resources were invested for the refinement and practice of the surgical process to meet the higher standards required.

b. The stereotaxic methodology

GCaMP6 mice (strain: FVB-Tg(Thy1-GCaMP6)5Shi., provided RIKEN BRC through the National Bio-Resource Project of the MEXT, Japan (Ohkura et al., 2012)), around 2 months of old of either sex, were implanted with two of our CMOS-based imaging devices (**Fig. 6A**). They were positioned adjacent to the CeLC and the DRN, both in either the left (formalin test experiment) or right (von Frey – formalin test experiment) brain hemisphere (**Fig. 6B**).

The mice were anaesthetized intraperitoneally (IP) with an anaesthetic mixture of Domitor, Midazolam, and Vetorphale (0.01 mL x bw in grams). Hair was removed from the top of their heads and the scalp was disinfected with 4% clorhexidine (Hibitane). They were restrained to a stereotaxic platform (SR-6M, Narishige) using earbars. A heating pad was provided underneath the animals to stabilize body temperature.

Skin was excised from the dorsal side of the head, just enough to access the implantation sites. The cranium was exposed by clearing away tissue and washing with PBS (Fujifilm Wako). After aligning the bregma and lambda, coordinates for the brain site targets were marked on the cranium (CeLC: AP: -0.8 mm, ML: -3.35 mm (left), DV: -4.0 mm; DRN: AP: -5.56 mm, ML: -0.35 mm (left), DV: -3.31 mm; all DV coordinates counted from the dura). All coordinates were determined using the Paxinos Mouse Brain Atlas (Franklin and Paxinos, 2008) and calibrated in previous trials. Two small micro-screws were shallowly secured into the cranium, spaced some distance from the marked sites. These provided additional anchorage for the dental cement used later.

Small cranial windows of around 1 mm in diameter were created on the targets using a dental drill (Hypertec II, Morita) and were cleansed of debris and blood with PBS.

The implants were clamped and aligned to stereotaxic manipulators (SM-15M, Narishige) and gently wiped with 70% ethanol (Fujifilm Wako) using cotton swabs and were secured. The manipulators were attached to the stereotaxic device rails and positioned properly. The devices were slowly lowered through the skull windows via the manipulator adjustment knobs, with the CMOS chip facing medially towards the target, up to the assigned depth. For the DRN, the path of implantation was angled as previously described (**Fig. 5b**). At this point, the manipulators were strictly prevented from further adjustments to maintain the proper implantation positions.

Once the targets were reached, the cranial windows were sealed with silicone elastomer (Kwik-Cast). Dental cement (Super-Bond kit, Sun Medical) was deposited around the manipulator-held devices and over the exposed skull and the surrounding incised skin, providing a protective seal. It was made sure that enough cement was used around and along the devices to provide strong structural support during the experiment proper wherein they will pulled by the movement of the mice. After the cement had set thoroughly, sufficiently holding the devices at the correct positions, the manipulator clamps were removed and the unconscious mouse was released.

The mouse was IP injected with Antisedan (0.01 mL x bw in grams) to reverse the effects of anaesthesia and was allowed to recuperate for at least 12 hours in a heated enclosure.

At the end of every experiment, the mice were sacrificed with an overdose IP injection of sodium pentobarbital (Somnopentyl, ~0.2 mL, KS Medical). They were perfused with a tubing pump (TP-10SA, AS ONE) with normal saline (Otsuka) and then 4% formaldehyde (Fujifilm Wako). Their brains were extracted and stored in 4% formalin overnight. Coronal sections of the brains (100 μm) were prepared using a vibratome (Linear Slicer PRO7, Dosaka) and were used to confirm successful targeting of the brain sites (**Fig. 6C**). Data from animals with unsuccessful implantations were disregarded.

A

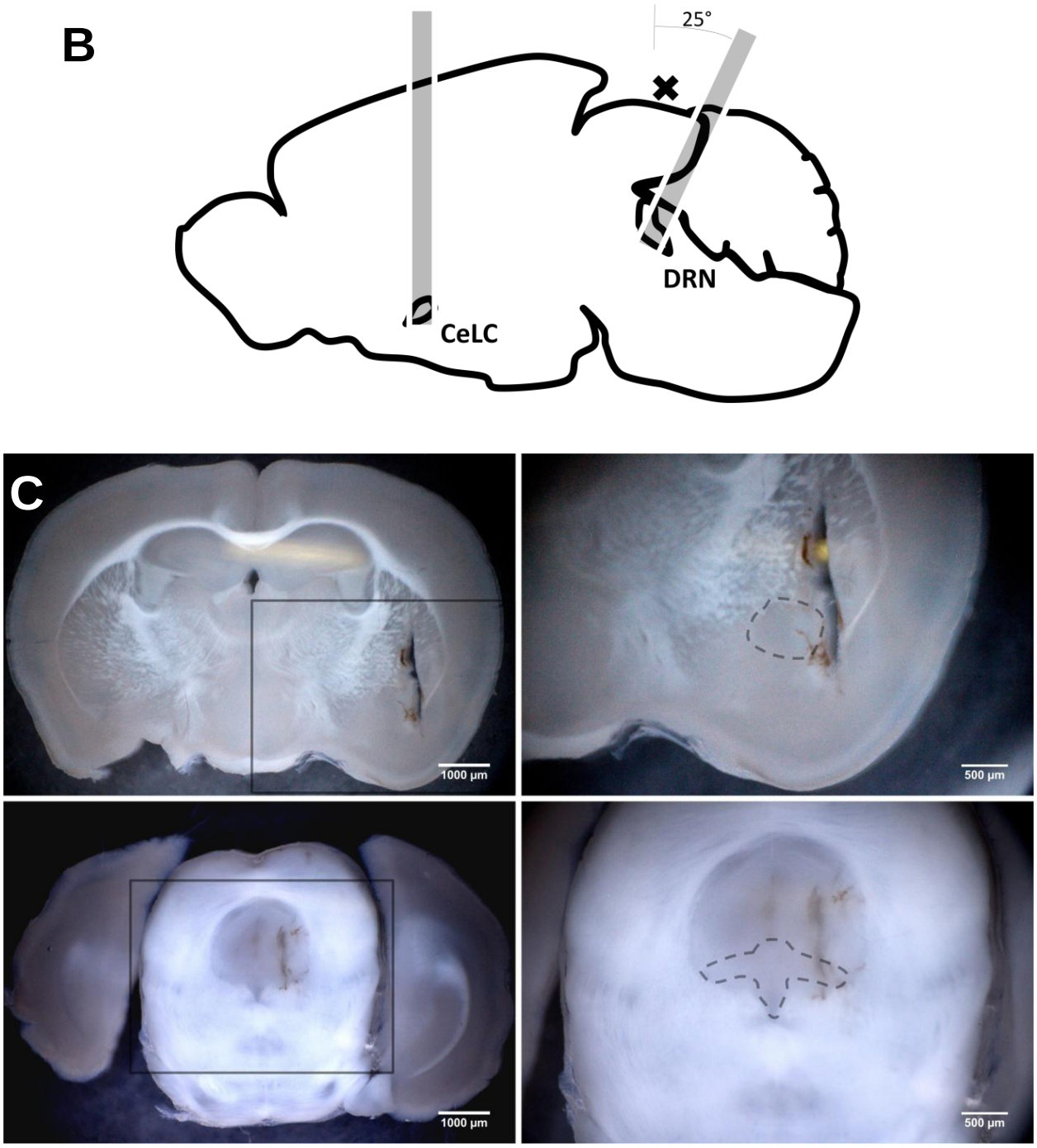

Figure 6. The implanted mouse and the paths of the implants to their targets. (A) Left and Middle: A mouse that has just underwent double-implantation, under anesthesia. Note the differing angles of the implanted devices; Right: Implanted devices attached to cables used for supplying power and collecting calcium-signaling

fluorescence data. (B) Paths of implantation through the brain. The cross (x) indicates the location of a large superficial transverse blood vessel on the brain's surface.(C) Coronal sections depicting lesions from implantations and the loci of the brain site targets. Lesions do not reach the dorsal brain surface because the sectioning and the implantation planes are not parallel, more so for the DRN targeting. Upper Left: AP: -1.58 mm, 25x; Upper Right: Zoomed in section from rectangle in upper left image, dashed line approximates the perimeter of the central amygdala (CeA), 45x; Lower Left: AP: -4.36 mm, 25x; Lower Right: Zoomed in section from rectangle in lower left image, dashed line approximates the perimeter of the DRN (dorsal, ventral, and lateral subsections), 45x.

4. Application on the Standard Formalin Test

a. Methodology

The Formalin Test

A modified formalin test was done with the aim of recording brain activity during pain perception, indicated by fluorescence from calcium signaling due to neuronal action potentials. Behavior attributed to pain perception, such as licking, was used to confirm the most likely source of the fluorescence imaging data (**Fig. 7A**).

The whole recording procedure was done within a darkened canvas tent. This is to prevent the interference of light from sources such as illumination lamps for animal handling, interior overhead lighting, and sunlight passing through windows. Light from such sources are of high enough intensity to permeate the very thin skull, and overlying layers, of the experimental mouse. Such light can still be detected by the implanted devices due to the high sensitivity of the CMOS imaging chip. The orbit and the frontal cranial bone are especially exposed to light penetration. Though the parietal cranium bone is covered with reinforcing dental cement, the cement itself is translucent

Implanted mice were anaesthetized with isoflurane (Fujifilm Wako) using an isoflurane pump (410 Anaesthesia Unit, Univentor). The implants were then connected to cables that were then connected to a slip ring. The rotating slip ring prevented entanglement of the cable pair and served as a bridge between the implants and the power sources (6146 DC Voltage Current Source, ADCMT) and collecting equipment (custom-made, NAIST).

After securing the connections, the mice were kept in an observation enclosure and monitored with a webcam (CMS-V37BK, Sanwa Supply). Illumination was under blue-light that was blocked by the blue-light filter and the red resist coating of the device. Their brain activity and behavior were recorded on a personal computer using specialized custom-made software (CIS_NAIST) and a webcam software (Bandicam) (**Fig. 7B**) for a minimum of 10 minutes to serve as a baseline. Afterwards, they were subcutaneously injected using a 30G needle with either 20μL 2% paraformaldehyde-PBS (Fujifilm Wako) ("**Formalin**" group (n=3)) or PBS (Fujifilm Wako) ("**PBS**" group (n=3)) at the plantar side of the right hind-paw, contralateral to the side of the implantations. Brain activity and behavior were recorded for a minimum of an hour. For the duration of the experiment, experimenters vacated the tent to prevent affecting behavior.

At the end of every experiment, the mice were sacrificed with an overdose IP injection of sodium pentobarbital (Somnopentyl, ~0.2 mL, KS Medical). They were perfused with a tubing pump (TP-10SA, AS ONE) with normal saline (Otsuka) and then 4% formaldehyde (Fujifilm Wako). Their brains were extracted and stored in 4% formalin overnight. Coronal sections of the brains (100 μm) were prepared using a vibratome (Linear Slicer PRO7, Dosaka) and were used to confirm successful targeting of the brain sites (**Fig. 6C**). Data from animals with unsuccessful implantations were disregarded.

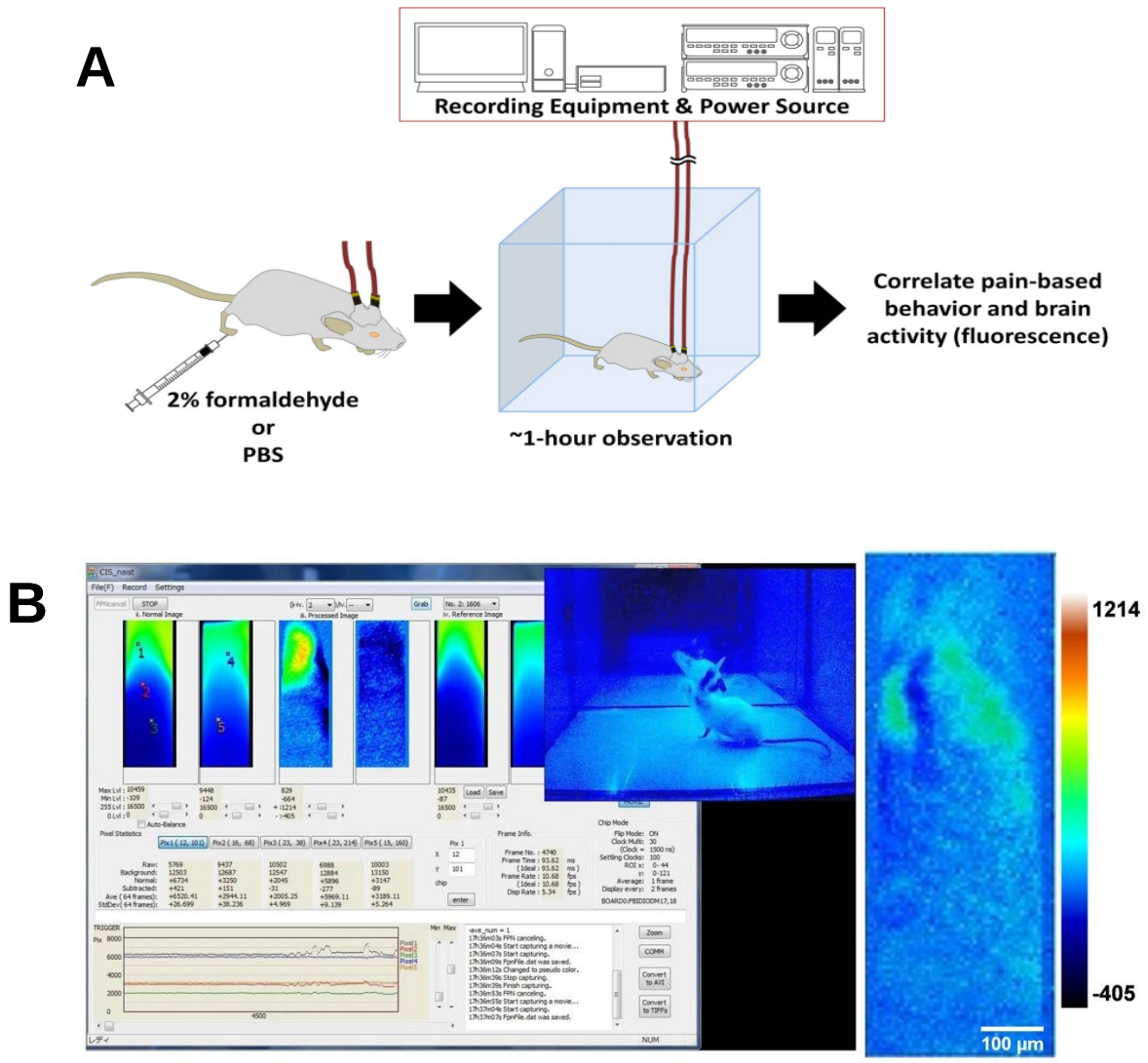

Figure 7. Formalin test with brain activity imaging. (A) The experimental design of the modified formalin test. (B) Left: Screenshot of the computer monitor during a formalin test. On the screen is the CIS_NAIST software that displays the windows (40 x 120 pixels, 300 x 9000 µm) for raw, processed, and reference frames of real-time video data, in pairs from left to right. The left of the pair is the fluorescence image from the CeLC, and the right of the pair is from the DRN. Also displayed are the fluorescence level traces at the bottom and frame number information at the middle right. The overlying the CIS_NAIST software window is the video feed of the mouse behavior from

the webcam; Right: A sample of a processed image of the CeLC with discernible fluorescent structures. Heatmap values are voltage values that represent ΔF.

Data Processing

Behavior recorded by the webcam was reviewed and pain-related behaviors were taken note of, specifically the licking of the injected site. Behavior was quantified by tallying the amounts of pain-induced licks on the affected paw per 2.5 minutes blocks within the 1-hour observation period. The results were graphed as a number of licks per time block.

Imaging data was acquired using CIS_NAIST, and saved as RAW files. The data was extracted from the files and analyzed using MATLAB (MathWorks). Custom made codes were written in order to process and visualize the data. For processing, the data was first stored as a 3-dimensional matrix (2D spatial pixel array across time), then separated into two for the CeLC and the DRN data. Afterwards, the period of injection was determined from webcam recordings, and also by looking at the offset frames in the averaged data set.

Removal of hum noise was performed by making a column vector containing the average values of each row in the pixel array. The average value of that was computed and subtracted to each element of the column vector. The resulting vector was subtracted to each column in the pixel array. This was done in each frame. That is, given a pixel reading $F_t(x, y)$ at frame t, where $x = 1{:}n_x$, $y = 1{:}n_y$, the following steps are performed for each t:

1. Form the column vector $\overline{x_t}$, where $\overline{x_t}(y) = \frac{1}{n_y}\sum_{i=1}^{n_x} F_t(i,y)$ for each $y = 1{:}\,n_y$.

2. Calculate $\overline{F_t} = \frac{1}{n_x}\sum_{j=1}^{n_y} \overline{x_t}(j)$.

3. Form the column vector h_t, where $h_t(y) = \overline{F_t} - \overline{x_t}(y)$.

4. The new reading $F_t^*(x,y)$ is then given by $F_t^*(x,y) = F_t(x,y) - h_t(y)$.

The data was normalized ($\Delta F/F_0$) by getting the average of the frames before injection as the baseline. That is, given $F_t(x,y)$, the baseline F_0 is given by $F_0(x,y) = \frac{1}{t^*}\sum_{t=1}^{t^*} F_t(x,y)$, where t^* is the frame number before injection. The normalized pixel reading $F_t^*(x,y)$ is then given by $F_t^* = \frac{\Delta F}{F_0} = \frac{F_t - F_0}{F_0}$, where $F_t^*(x,y) = \frac{F_t(x,y) - F_0(x,y)}{F_0(x,y)}$.

Based on a previously published study (Takehara et al., 2016), the approximate size of neurons was computed and the regions of interest (ROIs) were selected accordingly. Specifically, it was assumed that the maximum distance between a visible ROI and image sensor surface was 100 μm, and therefore; the full-width at half-maximum (FWHM) would increase 3-4 times compared to a distance of 0 μm. Given the soma and device pixel sizes (8-9 μm and 7.5 μm respectively) and the 4 times increase in soma size due to the distance from image sensor, then the ROI was computed to be around 6x6 pixels. Regions that seemed like neurons based on fluorescent activity were selected as ROIs for further analysis. The average of each ROI was plotted and compared against background values outside the ROIs. A scale bar representing 5% change from baseline was generated. A color plot showing the intensity of each pixel in

a frame was graphed to visualize the ROIs. The behavioral data was aligned with the calcium imaging data to see their relationship.

Afterward, the first-differenced calcium traces in each ROI were cross-correlated or auto-correlated. First-difference was applied to ensure stationarity of the data. That is, given a calcium trace reading z_t at time t, the first-differenced calcium trace Δz_t at time t is $\Delta z_t = z_{t+1} - z_t$. First-differencing was implemented using **diff()** function of MATLAB. Cross-correlation between CeLC and DRN ROIs was calculated by shifting the DRN data across time. That is, given the CeLC calcium trace reading x_t at time t and the DRN calcium trace reading y_t at time t, the non-normalized cross-correlation coefficient R at lag m is given by

$$R_{x,y}(m) = \begin{cases} \sum_{t=1}^{T-m} x_t y_{t-m} & m \geq 0 \\ R_{y,x}(-m) & m < 0 \end{cases}.$$

The (normalized) cross-correlation ρ at lag m is then given by $\rho_{x,y}(m) = \frac{1}{\sqrt{R_{x,x}(0)R_{y,y}(0)}} R_{x,y}(m)$. Here, $R_{x,x}(m)$ and $R_{y,y}(m)$ represents the non-normalized auto-correlation at lag m for x_t and y_t, respectively. The DRN time lag with the highest correlation with CeLC $m^* = \mathrm{argmax}_m\, \rho_{x,y}(m)$ was recorded as the best time lag.Cross-correlation analysis was implemented using **xcorr()** function of MATLAB.The three ROIs from CeLC and three ROIs from DRN were cross-correlated as follows: CeLC vs DRN, CeLC vs CeLC, and DRN vs DRN. Therefore, a total of 27 cross-correlations were analyzed per mouse.

To measure the relationship between brain imaging and behavior, the mutual information coefficient (MI) between these variables was computed. Basically, the mutual information coefficient (Cover and Thomas, 2006) between two (discrete) random variables X and Y is given by

$$I(X;Y) = \sum_{x \in \mathcal{X}} \sum_{y \in \mathcal{Y}} p_{X,Y}(x,y) \log\left(\frac{p_{X,Y}(x,y)}{p_X(x)p_Y(y)}\right).$$

Similarly, if X, Y are continuous, then the summation is replaced with integration. However, since brain imaging is a continuous random variable, while the behavior is discrete, MI was measured using an adapted method (Ross, 2014). MI was computed using **discrete_continuous_info_fast()** function of (Ross, 2014). Since the imaging data was a continuous real-valued dataset, it was binned and averaged across the same 2.5 mins window of the behavioral data. This enabled the measurement of mutual information between continuous imaging data and discrete behavioral data, where a higher value indicates more dependence between the two.

Finally, statistical analysis was done using MATLAB. Non-parametric tests were performed: Kruskal-Wallis test for the cross- and auto-correlation analysisand non-parametric two-way ANOVA (Friedman's test) for the brain calcium imaging and licking behavior relationship analysis were performed. P-values less than 0.05 were considered significant. Boxplots with median and interquartile range were graphed also using MATLAB.

Implanted Brain Temperature Measurement

To determine if the activation of LEDs can lead to brain injury and compromise the experiment, the inner-brain temperature, in Celsius, of an implanted mouse was measured during activation of the blue-light micro-LED at 0.5 mA. Two thermocouples (Cu/constantan (Type T) thermocouple, Muromachi Kikai Co., Ltd., Tokyo, Japan) were attached to needle-type devices with Parafilm M (PM-996, Pechiney Plastic Packaging). One thermocouple terminal was located by the LED and another at the device's insertion tip, serving as a reference site away from the LED. The thermocouples were connected to a digital compact microcomputer thermometer (BAT 700 1H, Physitemp Instruments LLC).

Mice were anaesthetized and implantations were done into the DRN of one mouse and the CeLC of another as previously described, but with some differences. After implantation, elastomer sealant was not used as a protective cover. Instead, PBS-moistened pieces of Kimwipe were applied on the exposed region surrounding the implant and were held in place with Parafilm. The animal's body temperature was allowed to stabilize. Temperature was recorded for 5 minutes before LED activation, for an hour during activation, and for 5 minutes afterwards.

Videos of the brain fluorescence activity were collected using CIS_NAIST and screen recordings of the working computer. Images of the fluorescence in the CeLC and the DRN were extracted from the time immediately after the injection of the substance and every 10 minutes thereafter, until the end of the 1-hour observation period. The clearest calcium imaging result was selected as a representative example of each sampling group.

b. Results

Calcium Fluorescence Imaging

No notable complications on the welfare of the experimental mice were encountered during the duration of the study. Implantation surgery was accomplished without issues and all the mice recuperated fully the following day. No signs of distress that may have come from the implantation were observed. Furthermore, there were no indications of encumbrance of the head. Post mortem weighing of the cement-bound dual implants, excluding the parietal portion of the cranium, gave an average weight of 0.474 g (n=5). The only signs of discomfort were the pain-related behavior and inflammation reaction of the Formalin group mice after injection and the slight agitation immediately resulting from animal handling.

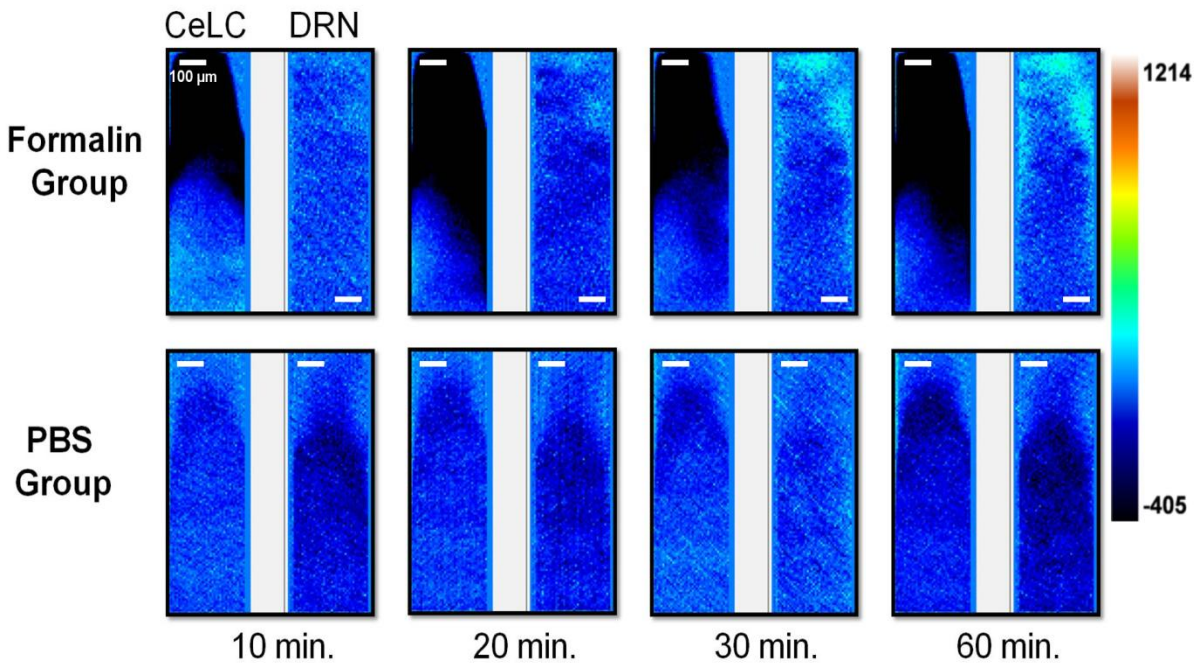

Figure 8. Brain activity fluorescence immediately after injection of formaldehyde or PBS. Neuronal fluorescence from the replicates that demonstrated detectable and distinct signals are presented. Time shown refer to the minutes that has passed after injection of the assigned substance. For all image pairs, CeLC is on the left and the DRN is on the right. Heatmap values are voltage values that represent ΔF.

Images of the calcium signaling from representative examples were chosen (**Fig. 8**). The top right corner of the DRN in the Formalin group had an increasing intensity throughout the time course, from the 20-minute mark onward, with distinct and prominent fluorescence. The CeLC of the same group, particularly the lower-left of the imaging area, initially displayed some fluorescence that gradually lessened over time.

On the other hand, the PBS group had more uniform and constant images across time. Slight changes in overall fluorescence can still be seen, such as a brighter DRN and CeLC at the 30-minute mark. The changes are quite difficult to spot by eye alone. Therefore, a more quantitative approach was taken.

Data Analysis

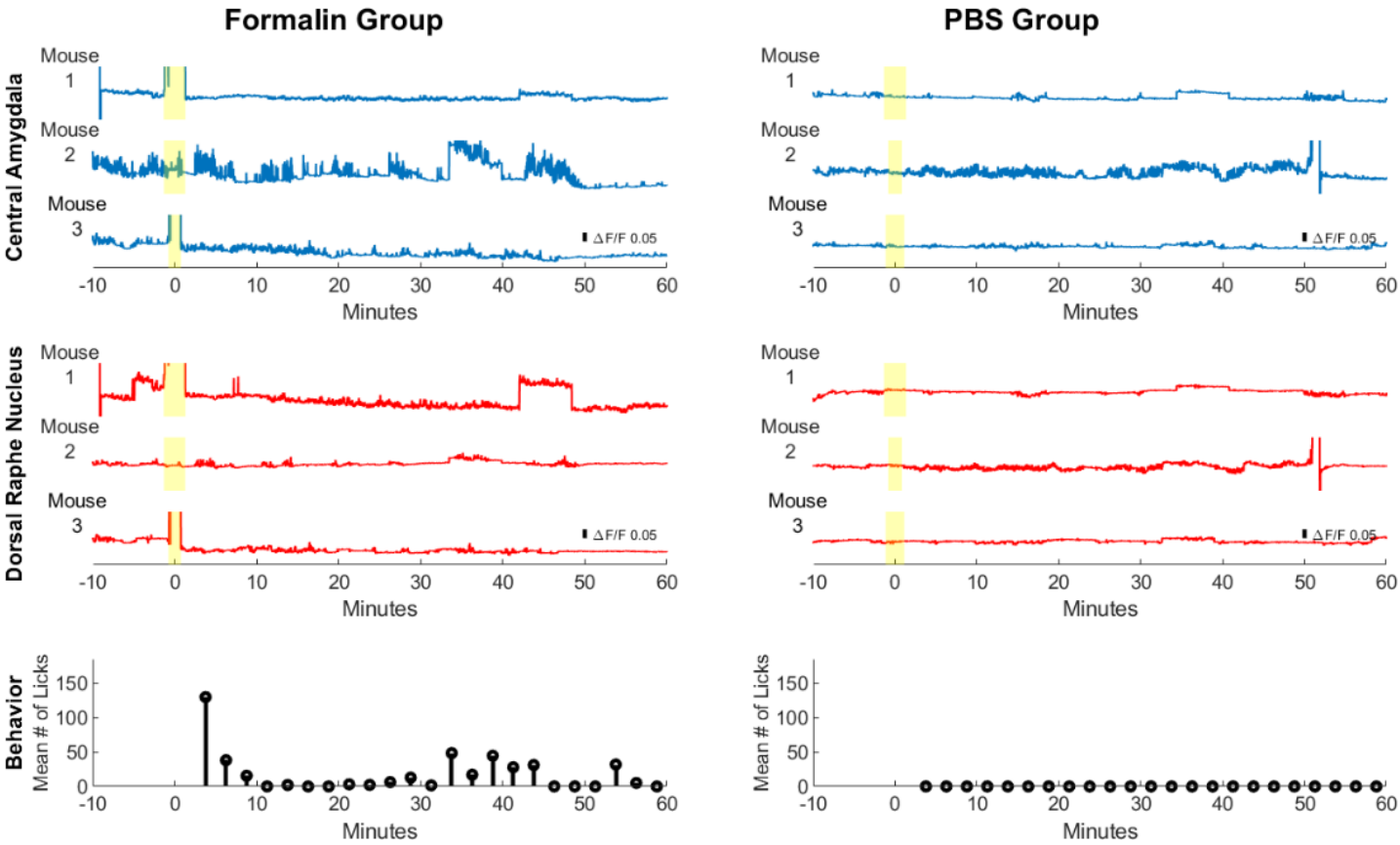

Figure 9. Calcium imaging and behavioral analysis across multiple mice. Brain calcium imaging and behavioral analysis of Formalin- and PBS-injected mice. The yellow highlight marks the injection period. The blue line graphs show calcium

measurements of the CeLC across multiple mice, while the red line graphs show calcium measurements of the DRN. At the bottom are the behavioral results for the average number of licks per 2.5 mins time block among Formalin mice (n=4) and PBS mice (n=3).

To better visualize changes in CeLC and DRN fluorescence activity, the whole frame average across time was computed in all mice (**Fig. 9, top and middle**). The sudden increase in fluorescence right after injection in the Formalin group can be an indicator of acute pain. In addition, the paw-licking behavior of the mice was also measured simultaneously (**Fig. 9, bottom**). Based on the $\Delta F/F_0$ scale bar, the Formalin group generally had higher amplitudes than the PBS group. For example, Formalin Mouse 2 displayed higher fluorescence values compared to PBS Mouse 2 in the CeLC. Furthermore, Formalin Mouse 1 had higher fluorescence intensities than PBS Mouse 1 in the DRN. In addition, the Formalin group had higher frequency of fluorescent peaks for both brain sites. This was most apparent for Mouse 2 and 3 for CeLC and Mouse 1 for DRN. Conversely, the PBS group had graphs that are comparatively flatter. Since this was a proof-of-concept to show that the dual-implantable device works, more mouse samples and further analysis can be done to quantify the difference in amplitudes and frequencies between both groups.

Pain-related behavior was observed from all the mice of the Formalin group, as reflected by the average number of licks. A high number of licks was seen in the initial minutes after injection. The licking behavior then subsided after 10 mins. Then, after 30

mins licking behavior started to increase again. This bi-phasic response may correspond to the acute and inflammatory phase of formalin injection, as will be discussed later. Interestingly, peaks in licking behavior also corresponded to higher fluorescence activity in the CeLC and DRN. On the other hand, the PBS mice displayed very little hindpaw-licking behavior, if any at all. Because of the very small behavior count for this group, the average all throughout is very close to zero.

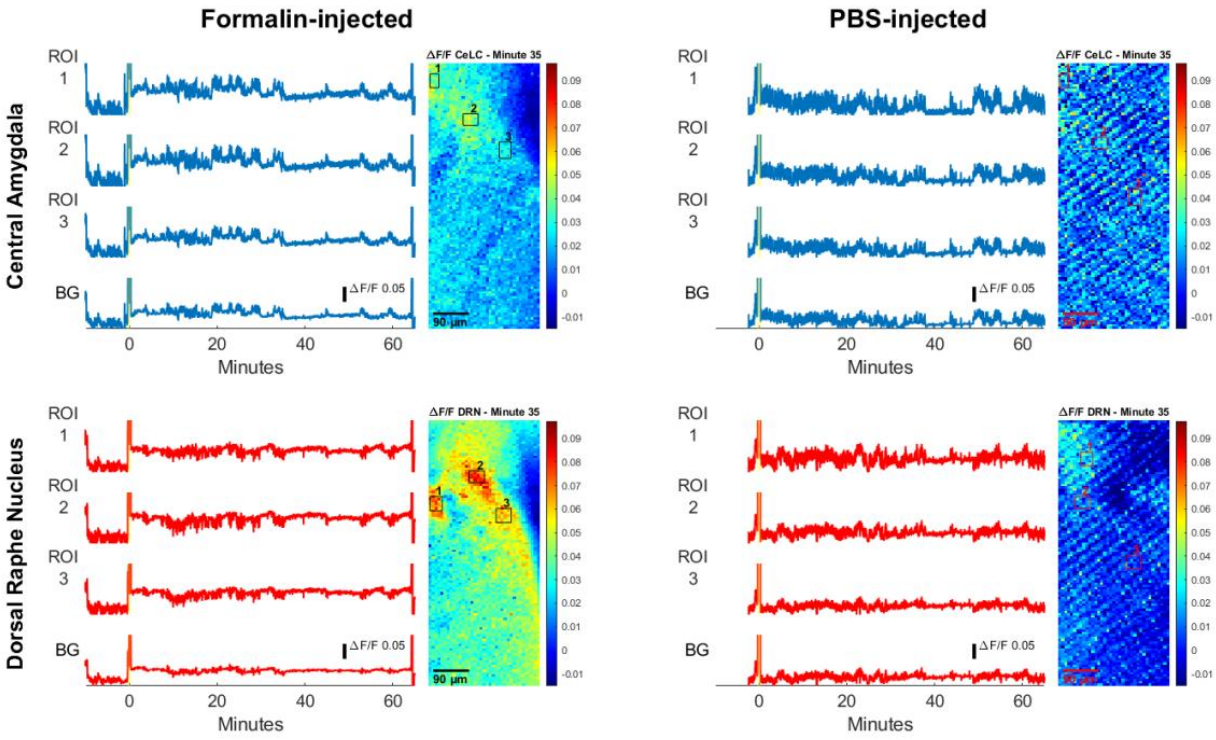

Figure 10. Calcium traces of specific regions of interest (ROIs). Calcium measurement of Formalin-injected mouse and PBS-injected mouse. The ROIs measure at around 6 x 6 px. The yellow bar on the line graph marks the injection period. The blue line graphs show measurements in the CeLC, while the red line graphs show measurements of the DRN. The background values (BG) are the average of all the

pixels outside the ROIs. Beside the line graphs are images of sample frames where ROIs are enclosed in black or red boxes.

Another two mice were selected as representatives, one per sampling group, to visualize analysis of multiple regions of interests (ROIs) (**Fig. 10**). Slight differences in timing and intensity of fluorescence can be seen in ROIs of the same brain region. For instance, in the Formalin-injected mouse, DRN ROI2 displayed more fluorescence activity than DRN ROI1 at the 20-minute mark. It is also observable that the ROIs of the DRN have higher and more distinct spikes than the background. Furthermore, ROI 1 and 2 of the CeLC had higher fluorescence amplitudes than ROI 3. However, CeLC ROI 3 still had higher fluorescence than the CeLC background values.

On the other hand, the PBS-injected mouse had ROI values that are relatively similar with the background. Similar to Figure 5, the PBS mouse had a more constant fluorescent activity where its peaks do not deviate too far from the average noise value. The peaks of the Formalin-injected ROIs were more distinct and had higher amplitudes compared to its baseline level before injection.

Formalin Mouse 3

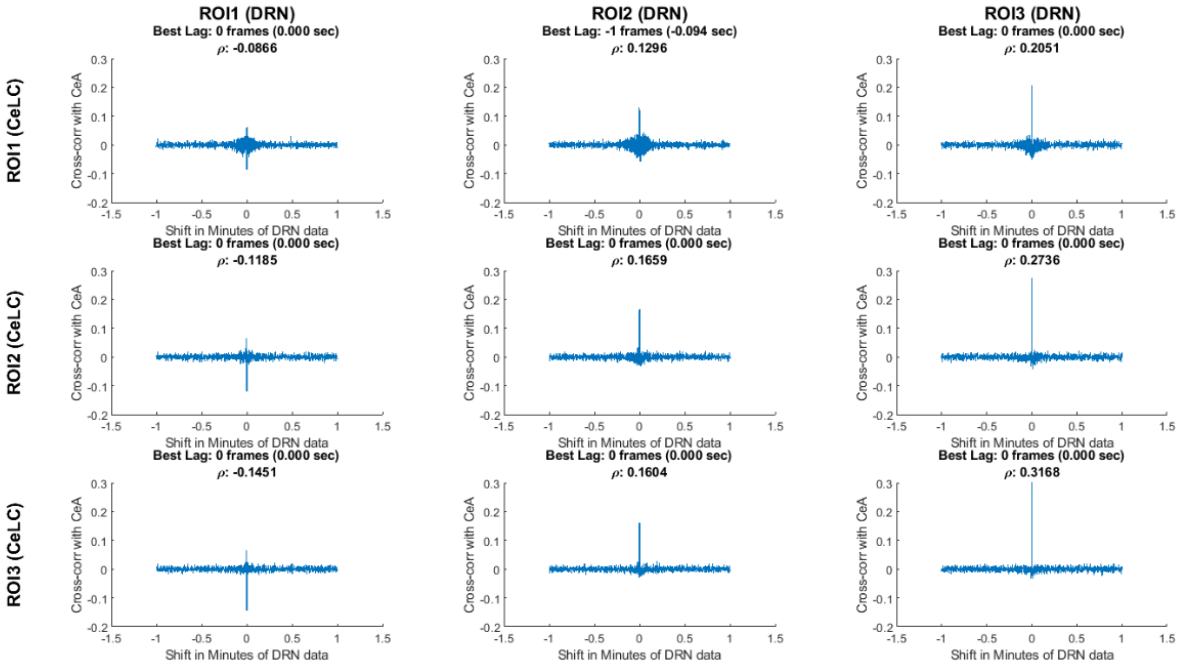

PBS Mouse 3

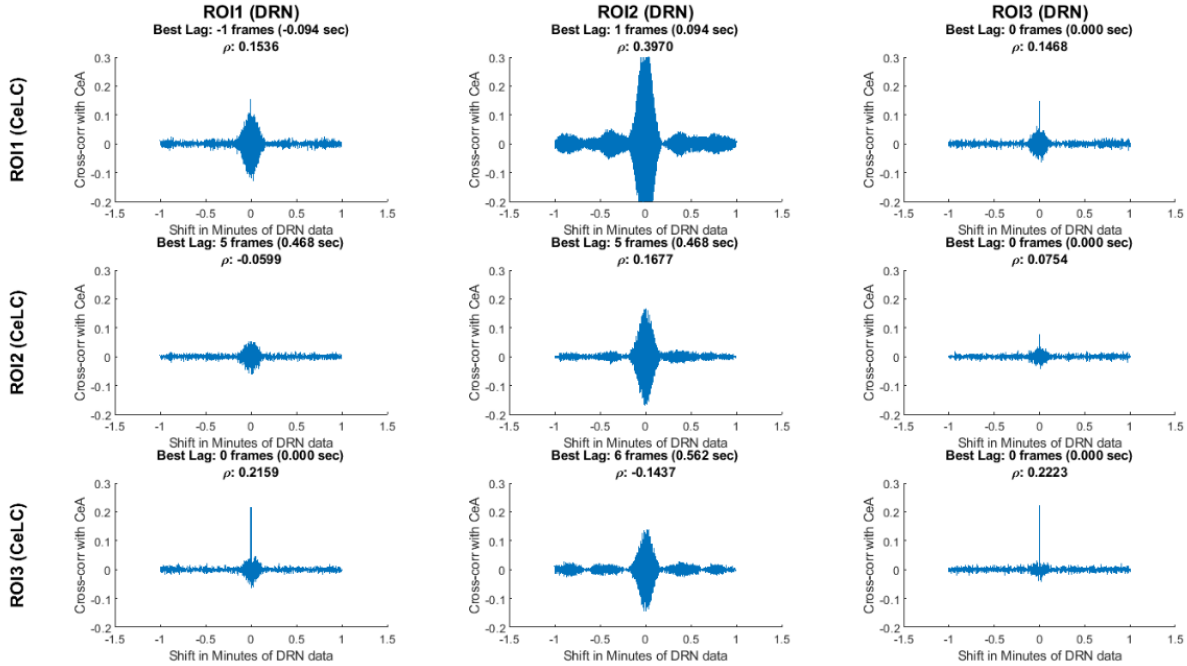

Figure 11. Cross-correlation analysis of two representative mice. Top: Formalin-injected mouse; bottom: PBS-injected mouse. The figure shows the cross-correlation of the first-difference of CeLC fluorescence imaging data with DRN data. The correlation between CeLC and time-shifted DRN (across varying lags) is measured. Peaks indicate high cross-correlation at that specific shift or time lag of the DRN data. The time lag with the highest cross-correlation coefficient (ρ) is indicated at the top of each graph.

The relationship between each ROI was explored. The small size and large field of view of the device made it possible to measure cross-correlation of multiple ROIs within and between the CeLC and DRN. First, cross-correlation analysis of the Formalin-injected mouse showed distinct and clear peaks mostly at time lag 0, meaning there was no almost no delay in the timing of their firing or activation (**Fig. 11**). This is indicated by the narrowness of the graphs. The only exception was the cross-correlation between CeLC ROI 1 and the DRN ROI 1. The data indicated that when the first-differenced DRN data is shifted 1 frame back, then the correlation with first-differenced CeLC data increases. This means that when the CeLC fluorescence increases, there is a positive correlation that the DRN fluorescence will also increase after 0.094 s. However, this was only true for one ROI of the CeLC. The other two ROIs of the CeLC showed a definite peak at 0 time lag, which indicated that the cross-correlation was highest at 0 s delay.

In contrast, the PBS-injected mouse had less clear and less distinct cross-correlation peaks. It can be seen that most of the cross-correlation graphs are broader,

especially for DRN ROI 2. Furthermore, the best time lag is less consistent among the ROIs, with one pair having the highest cross-correlation at 6 frames (0.562 s) and two pairs of ROIs at 5 frames (0.468 s). This may indicate less synchronization between CeLC and DRN neuronal firing in PBS-injected mouse.

A

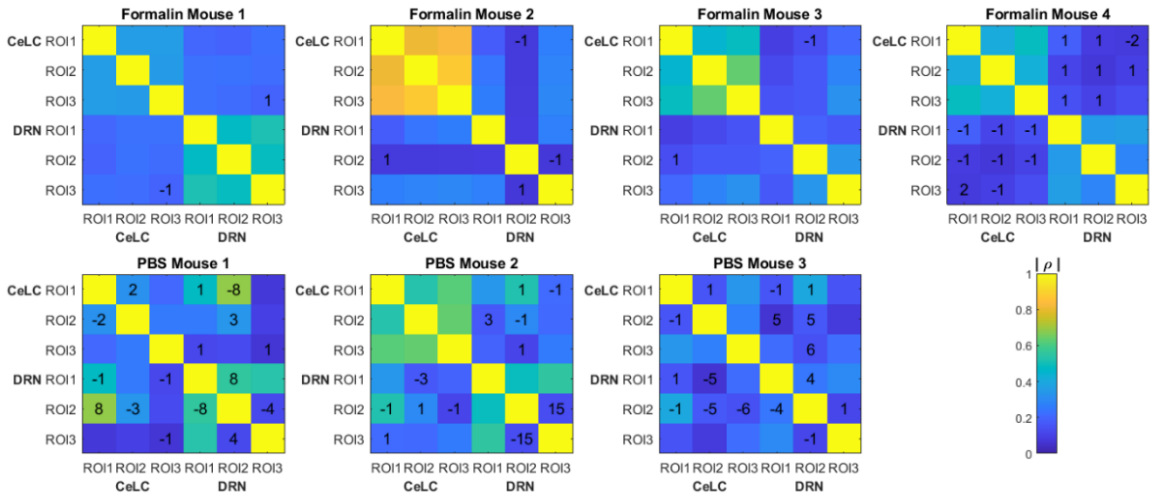

B

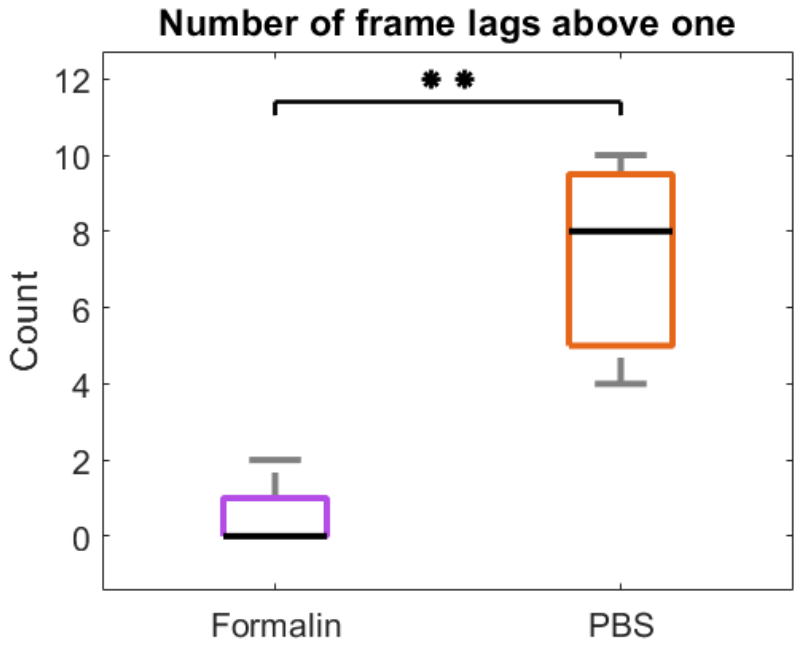

Figure 12. Cross- and auto-correlation analysis in all mice. (A) Heatmap showing time lags with the highest cross-correlation coefficients. ROIs from CeLC and ROIs from DRN in each mouse were cross-correlated. The values written indicate the time lag of first-differenced DRN data in frame number that showed the highest cross-correlation with the original unshifted first-differenced CeLC data. No value means the best lag was at 0. The color indicates the cross-correlation coefficient (ρ) from low (blue) to high (yellow) in absolute values. (B) Box plot of the number of frame lags that were above 1 in both treatment groups. Kruskal-Wallis test was performed and a significant difference was computed (**$p = 0.00773$, $\alpha = 0.05$).

To provide more insight and see if the results are consistent, the cross-correlation of ROIs in each mouse was analyzed (**Fig. 12**). Majority of the peak cross-correlations in the ROI crossings in the Formalin group mice was at time lag 0, indicated in the boxplot matrices as empty cells (**Fig. 12A**). However, it can be observed that PBS mice had several non-zero and non-one time lags. For example, PBS Mouse 1 had a high cross-correlation ($\rho = 0.69$) at -8 frames when analyzing between its CeLC ROI 1 and DRN ROI 2. Then its CeLC ROI 2 and DRN ROI 2 had the best lag at +3 frames. Furthermore, even within the DRN, there was a high cross-correlation at 8, 15, and 4 frame lags for PBS Mouse 1, 2, and 3 respectively. On the other hand, more cross-correlations at time lag 0 can be seen in Formalin-injected mice. For instance, when comparing within the same brain region (ie. CeLC vs CeLC or DRN vs DRN) all ROIs displayed a best time lag of 0, with the exception of DRN ROI 2 and 3 of Formalin

Mouse 2. Taken together, this may indicate less synchronization within the DRN of PBS-injected mice.

To compare the difference between the number of frame lags higher than 1 for each mouse group, a two-tailed unpaired t-test was performed. The number of frame lags higher than 1 was statistically higher in the PBS group compared to the Formalin group ($p = 0.00773$, Unpaired t-test). This confirmed the hypothesis that PBS-injected mice had a higher number of ROIs that were not as synchronized compared to the Formalin-injected mice.

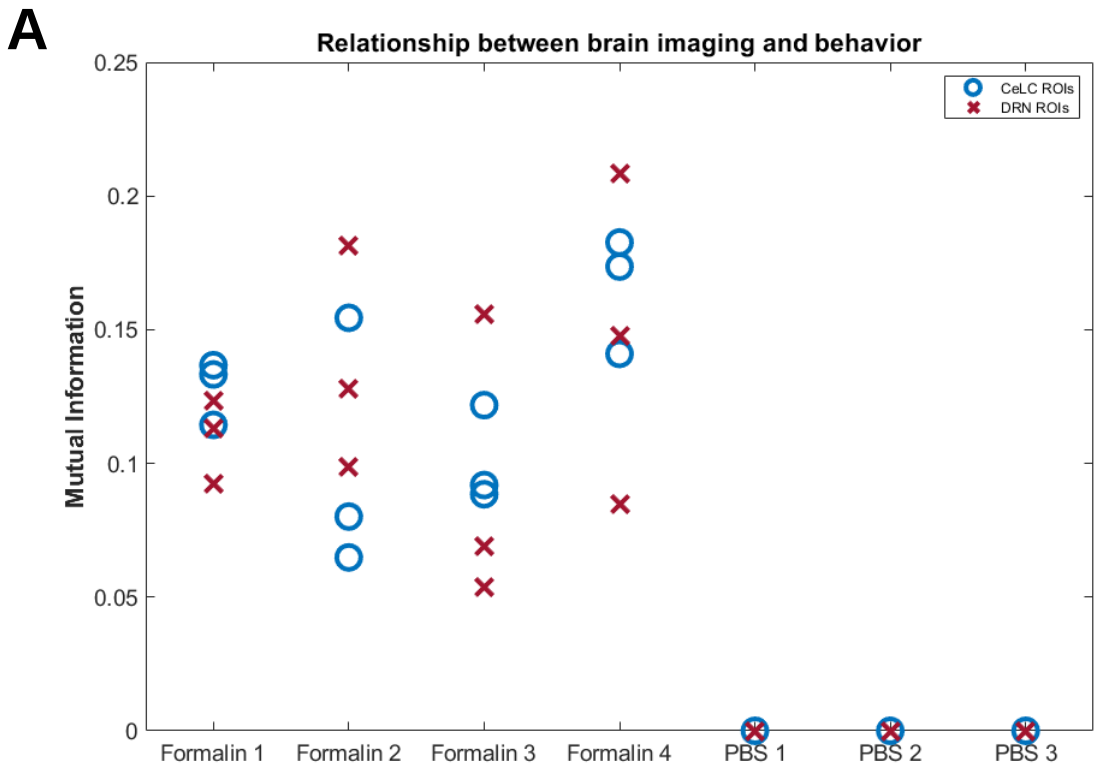

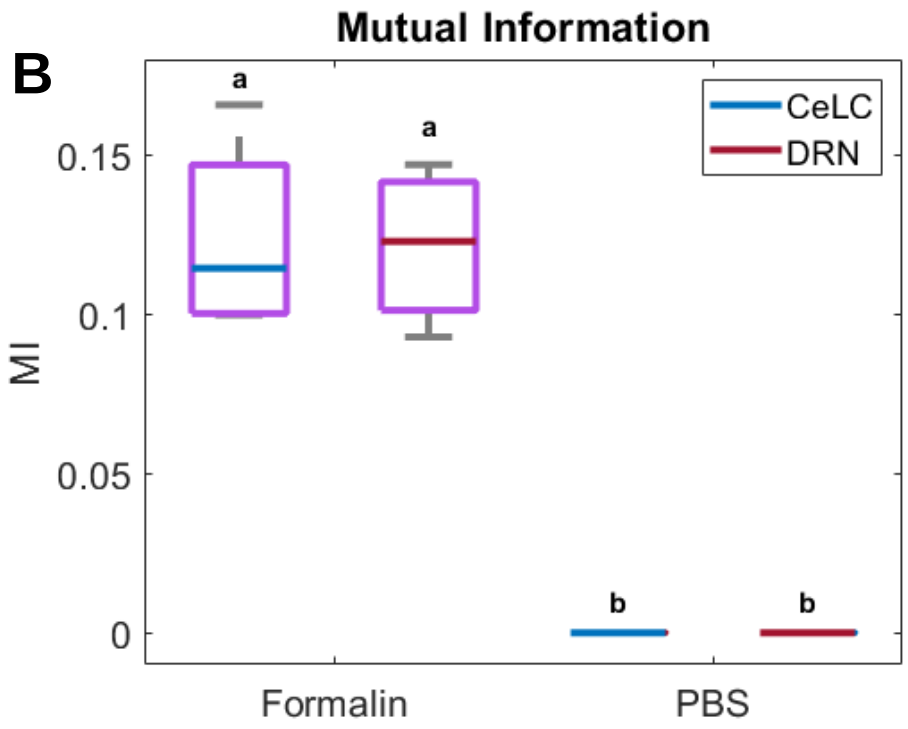

Figure 13. Relationship between brain calcium imaging and licking behavior. Relationship between brain calcium imaging and licking behavior. (A) Plot of mutual information between imaging and behavior. Blue circles indicate ROIs from CeLC, while red crosses indicate ROIs from DRN. (B) Box plot of the mutual information (MI) when ROIs in each mouse were averaged. PBS mice showed almost 0 MI with behavior, while Formalin mice showed higher MI values. Non-parametric two-way ANOVA showed significant difference between Formalin and PBS groups ($p < 0.05$, $\alpha = 0.05$), but no significant difference between CeLC and DRN within each group.

Finally, to measure the relationship between the brain calcium imaging data and licking behavior of mice, we calculated their mutual information (MI). The MI between calcium imaging of PBS mice and their licking behavior is close to 0, showing almost no

relationship. On the other hand, the Formalin mice displayed higher MI levels across different ROIs and brain areas (**Fig. 13A**).This was further confirmed using two-way ANOVA, wherein the Formalin group was significantly different compared to the PBS group ($p < 0.05$). However, no difference was detected between CeLC and DRN within each group.

By using this MI metric, the capability of the dual-implantable device to correlate brain activity and behavior was demonstrated. This showed the potential of the device for use in further experiments and analysis.

Temperature Recordings

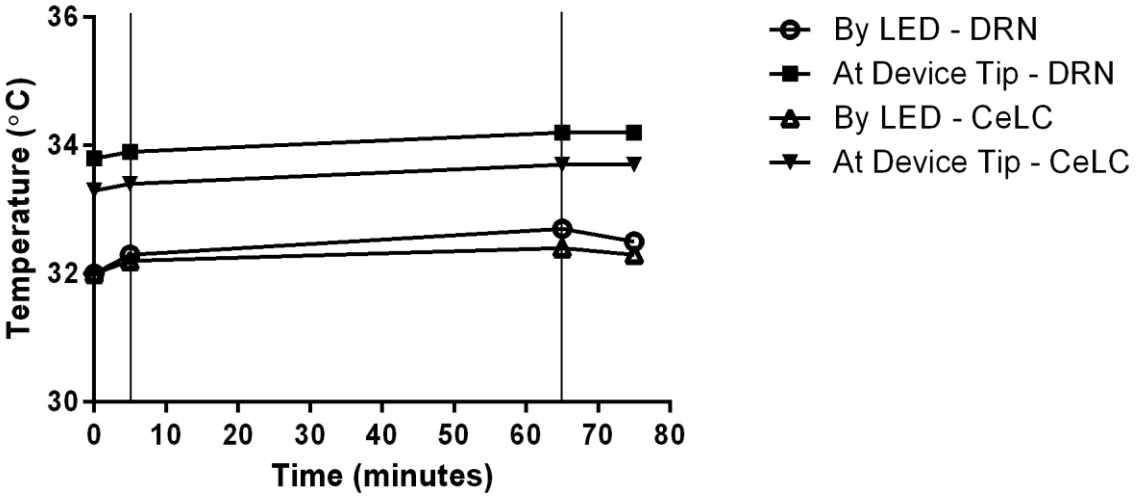

Figure 14. Recorded change of DRN and CeLC temperatures during implantation. Temperature readings were done in the vicinity of the implanted devices, specifically by the LED and at the device insertion tip. Thin vertical lines in the graph indicate start and end points of LED activation time.

Temperature readings in a double-implanted mouse indicated a very small increase in deep brain tissue temperature during activation of the blue-light micro-LED (**Fig. 14**). At most, there was 0.5°C increase in the portion of the DRN next to the LED. The results also show that proximity to the LED does not necessarily lead to a higher tissue temperature.

c. Discussion

It has been demonstrated that the use of our device in a double-implantation set-up is feasible and will not introduce complications that can affect animal welfare. All trials proceeded successfully with no mice displaying signs of excessive distress or injury from the implantation. Additionally, internal or core brain temperature of the implanted mice are well within the normal physiological levels of rodents, with the maximum limit at around 38°C (Yarmolenko et al., 2011; Mei et al., 2018). This is true whether the LED was activated or not. Along with the very minute increase in temperature during LED activation, temperature-related necrosis can be said to have not occurred. The relatively low internal body temperature can be attributed to the sleeping state of the recorded mouse (Sela et al., 2021). With the devices' viability and novel features, many methodology changes can be explored. It is important to note that these statements are only applicable to short-term set-ups, those lasting for a few days per run. Nevertheless, the use of the device is still very safe for many methods.

The qualitative (**Fig. 8**) and the quantified averaged whole-frame calcium imaging results (**Fig. 9**) have shown that there are perceivable differences in the fluorescence

levels between the Formalin-injected and the PBS-injected group. The increase in signaling of the former group can be attributed to nociception itself. The higher fluorescence signal intensity of the Formalin group clearly corresponds to the elevated averaged levels of pain-related behavior (amount of injected paw licking/tending per 2.5 minutes) which is the indicator of pain sensation. It is to be interpreted that the higher the frequency of the licking, the more intense is the pain being experienced.

The formalin test is a method that can induce a bi-phasic response to pain: an early acute phase (0-5 minutes post injection) and a later tonic or inflammatory phase. The acute phase pain comes from the tissue damage from the injected formaldehyde and the tonic phase pain is from the response of the immunity system to said damage. The latter phase seems to occur around 15 minutes (Hunskaar et al., 1985; Hunskaar and Hole, 1987; Shibata et al., 1989; Rosland et al., 1990) until 60 minutes post injection (Manning and Mayer, 1995a). This is also dependent on the effects of environmental temperature on the potency of inflammation (Rosland, 1991; Tjølsen et al., 1992). The vast range of the timing is reflected in the flattened second peak in the averaged behavior data of the Formalin group (**Fig. 9, bottom**). Nevertheless, the biphasic pain response is still clearly observable in the intensity peaks of the whole-frame fluorescence graph and especially in the behavior response tally of the Formalin group (**Fig, 9, left side**). The peaks of both data sets can also be matched in terms of timing, further supporting that they do actually represent the same thing, the presence of pain.

Though the trend is not wholly consistent among mice, there are discernible and distinct patterns and shapes that can still be observed using our new device. In the

images, these fluorescent forms or shapes can be distinguished with varying degrees of effort, especially in that of the DRN of the Formalin group. This determination of separate and distinct forms is the basis of ROI selection from the data collected by the CMOS-based device. These forms are surely not individual neurons. They are much larger than the widest span (9 – 10 μm) of an average soma of neurons found in the selected sites. Light scattering through the tissue cannot be discounted as contributing to the size of the forms as seen on the images, but their effects are assumed to be minimal (Takehara et al., 2016). They are possibly neuronal clusters or ganglia and not glial cells because of the nature of GFP expression in GCaMP6 mice. The actual identity of these fluorescent forms is hard to ascertain because of the low resolution. This is an unavoidable limitation in the use of the CMOS imaging chip that is without a lensing or focusing material. Thus, it can be concluded that the 6 x 6 px ROIs used in the correlation analyses most likely contains a multitude of neurons and the fluorescence recorded within that ROI is the collective firing of said neurons.The CeLC is a major component of the pain matrix. It has context-specific paradoxical roles of promoting hypoalgesia (Manning and Mayer, 1995a, 1995b; Kang et al., 1998; Finn et al., 2003; Sabetkasaei et al., 2007; Yu et al., 2007; Veinante et al., 2013) and hyperalgesia. Hyperalgesia is accomplished during inflammation (Carrasquillo and Gereau, 2007; Veinante et al., 2013). Meanwhile, the DRN has also been shown to have an inflammation-specific antinociceptive function (Palazzo et al., 2004; Cucchiaro et al., 2005). Their inflammation-induced activation and the slightly variable tonic phase timing might explain the persistent activity spikes of both sites in the Formalin group. This is reflective of the flattened, prolonged second peak, representing the tonic phase,

in the Formalin group's behavior data. This does not apply to the first distinct peak of the acute phase. Even if both the fluorescence and the behavior data are indicators of pain perception, the two data sets may not be total complements to each other because of the complex effects of formalin-induced nociception. Even so, together they still provide a holistic portrait for visualizing pain.

The qualitative visual data of the ROIs also echoes the results of the behavior analysis. The images of both brain sites, more so the DRN, of the Formalin group display ROIs of higher fluorescence intensity compared to the PBS group. The difference becomes less apparent, especially for the CeLC in the latter half of the observation period. The CeLC was expected to fluoresce more prominently, following its central role in modulating pain perception. This weak response to pain stimulation can be attributed to the lateralization of the CeLCs of the two hemispheres. The right CeLC has been observed to be more responsive to nociception to a greater degree (Ji and Neugebauer, 2009; Allen et al., 2021), though this does not mean that the left CeLC is fully inactive (Allen et al., 2021). The descending architecture of the CeLCs are ipsilateral, especially the left one (Manning, 1998; Ji and Neugebauer, 2009). Since the study investigated the left brain hemisphere and induced pain contralaterally, the resulting calcium signaling could not have been strong. The fact that the devices have still detected pain-based trends in fluorescence between the two groups demonstrates its sensitivity.

In the quantification and graphing of calcium imaging of the PBS group ROIs, there are high frequency, but lower intensity, traces. It is apparent in the images for this group that there is a high amount of signal noise that could have contributed into this.

Because of the method of deriving the final fluorescent values of the ROIs from the deviation from the background signals, including the noise, it is of great concern that the noise values were not sufficiently subtracted or removed. This suggests that a more thorough spatial filtration method is required, applicable to ROIs, to smoothen the signals graph further to an acceptable degree. Even though the data as is was sufficient enough to demonstrate differences in the ROI imaging values between the sampling groups, further processing can demonstrate the trend more clearly.

Cross-correlation analysis showed that the Formalin-injected mice had more max cross-correlations at time lag 0.The closer it is to zero, the less there is a timing delay in the firing of the ROIs, and the more synchronized are their activity. Though some ROIs displayed best lags at 1 or 2 frames, most other ROIs showed more synchronous activity. In contrast, the PBS-injected mice had more varying frame lags with several values higher than 1 frame delay/advance. The analysis indicated that there may be more asynchronous firing between CeLC and DRN neuronal firing in PBS-injected mice unlike the Formalin-injected mice. This suggests a coupling mechanism between or within the CeLC and the DRN during pain processing. The same mechanism is present in the adjacent cells of the dorsal root ganglion (DRG), a downstream neural pathway of the CeLC and the DRN, during inflammation and nerve damage (Kim et al., 2016). This synchronization was less apparent in naïve mice not exposed to pain.

Additionally, the highly variable time lag values of the cross-correlation coefficients of the ROIs portray a heterogenous population of neurons of differing roles in pain perception. For instance, the central amygdala can increase or decrease pain-related behavior depending on the cell type. Cells expressing protein kinase C-delta

played a role in sensitization to nerve injury and increased pain response, while cells expressing somatostatin were inhibited and drove anti-pain behavior (Wilson et al., 2019). Furthermore, adjacent DRN 5-HT neurons are closely coupled and synchronized; however, non-adjacent 5-HT neurons are not. Also, there is a difference in the auto-correlograms of serotenergic and non-serotnergic neurons in the DRN, where non-5-HT cells are more irregular while 5-HT cells are more periodic (Wang and Aghajanian, 1982). Our analysis demonstrates such heterogenous interactions and behavior as well because ROIs within the same brain region, particularly the DRN of PBS mice, showed varying cross-correlograms. In addition, cross-correlation between CeLC and DRN ROIs had different time lags even if the mice were in the same treatment group.

The large gap in the tallied pain-based licking behavior of the groups confirms the successful execution of the formalin test, with the PBS group displaying none. This is reflected in the difference in calcium signaling between the Formalin and the PBS groups, though the peaks of the behavior tally graph and the fluorescence graph do not match after the initial phase. So, even though PBS Mouse 2 demonstrated relatively high CeLC brain activity, it is not indicative of any pain processing, based on behavior. This is further supported by and elucidated in the MI analysis between behavior and calcium signaling result.

MI is the amount of shared information between the two data, and shows how related they are with each other. A value of 0 indicates that the two data are independent. MI has several advantages such as being unbiased to the sample size, being model independent, being unrestricted to the data type, being able to detect linear

and non-linear interactions, and being multivariate (Ross, 2014; Timme and Lapish, 2018). This metric is a dependable measure to support the assumption that the brain-activity fluorescence data is reflective of the pain-expression behavior data. The analysis showed that the MI between calcium imaging of PBS mice and their licking behavior is close to 0. This means that the imaging data is almost not related to any behavior in the PBS-injected mice. The detected brain activity in the PBS group mice is very likely not of pain perception. In contrast, the Formalin mice displayed significantly higher MI levels. Because the MI value is well above zero, it can be soundly claimed in this group that a relationship does exist between fluorescence and behavior. The variable MI values for the DRN and the CeLC, showing no trend, means that the neither of the brain regions' activity corresponds more to the expression of pain. They are most likely both relevant to pain processing, though to different degrees, as apparent in the higher calcium imaging intensities for the Formalin group brains. Though, even if a miniscule MI value was computed from the data sets of the PBS-injected mice, since there was no tallied pain-related behavior it can be argued that the MI analysis is very weak and should be invalidated. If taken this way, it will also make the MI statistical analysis of the two groups invalid. Even so, the average MI coefficient for the Formalin group alone is still relevant. The non-zero MI reinforces the assumptions that the calcium imaging of this group is related to the pain-indicating behavior and that the imaging is a direct representation of pain processing. Overall, data analysis demonstrated that this significant gap in MIs between groups is indicative of the correlation between elevated calcium imaging in pain processing regions and increased expression of pain-based behavior.

Previous in vivo investigations on the mechanisms of pain, using calcium imaging, have mostly been done on the spinal cord level, as a necessity for less injurious methods of visualizing neural activity (Anderson et al., 2018; Miller et al., 2018; Xu and Dong, 2019) (Anderson et al., 2018; Miller et al., 2018; Xu and Dong, 2019). Our study is one of the first attempts to simultaneously image pain processing at two relevant brain regions in vivo, addressing the need for multi-site visualization for neuron-network studies (de Melo Reis et al., 2020).

d. Summary

A standard pain experiment, the formalin test, was modified and executed with transgenic GCaMP6 mice double-implanted with the CMOS-based calcium signaling fluorescence imaging implant. The imaging targets are two brain regions involved with pain processing: the CeLC and the DRN. The feasibility of the method was gauged with two considerations. The first is that no injury, excessive burden, and additional pain should derive from the double-implantation process. The second is that the fluorescence signals collected should correspond to the established results of the test and the pain-related behavior exhibited by the mice.

Monitoring of the experimental animals have shown that the double-implantation method did not cause any physiological conditions that might hamper with the procedure of the pain experiments. The mice's movement and behavior was unrestrained by any excessive weight or pain. There were no intense temperatures recorded inside the mouse brain with activated devices.

The collected fluorescence data has shown a significant difference between pain-induced and the control group. This is further corroborated by data analysis and the matching with quantified behavior. The bi-phasic pain response was also reflected in the brain reading data.

The experiment has shown that the use of the devices in a double-implantation set-up as applied in a well established pain experiment is very possible and with minimal risk. The findings have established that there is much potential in other applications in the use of the CMOS-based needle type devices, especially in studies as sensitive as those involving pain perception and processing.

5. Application on the Modified von Frey – Formalin Test

a. Methodology

Further methods on the usage of the CMOS-based needle-type fluorescence imaging device was explored with a hybrid of two tests: the von Frey tactile sensitivity test and the previously executed formalin pain test. This combined method will from here on be referred to as the von Frey – formalin test. The von Frey – formalin test is a method that investigates hyperalgesia, the heightened sensitivity to tactile stimulus, or simply touch, arising from persistent pain. In this method's case, the pain utilized will be inflammatory, from the latter/tonic phase of the formalin test.

As established in my previous work, fluorescence signals in the pain-processing brain regions of GCaMP6 transgenic mice are an indicator of the process of nociception or the downstream processes deriving from it. In this work, it was my aim to determine if hyperalgesia can also be reliably determined with fluorescence signals collected by our devices using the same set-up as previous, but modified to accommodate the tactile stimulation process. If proven so, it would demonstrate flexibility in the manner of the usage of the devices and the potential of the device for use in other related methods.

The experiment proceeds very similarly as the previously described modified formalin test, but with additional steps and alterations to the set-up and the formalin and PBS administration site (**Fig. 15A**). The most prominent changes in the equipment used are with the enclosure and surface holding the experimental animal. During the experiment, the mouse is enclosed in an acrylic cylinder with covered sides with a diameter small enough to prevent pacing. Movement must be limited to make the tactile

stimulation process easier to perform. Throughout the procedure, the enclosed mouse rests upon a raised PVC-tube platform with a plastic mesh floor. The gauge of the mesh is enough to support the mouse comfortably, but with openings wide enough to allow for tactile stimulation with von Frey filaments or aesthesiometers (Aesthesio Von Frey Filament Set, BIOSEB Lab Instruments) (**Fig. 15B**). The underside of the mesh platform was illuminated with blue-tinted light and monitored with a webcam. For this experiment, the right hemisphere CeLC and DRN were targeted for imaging and the plantar side of the left hind paws of the experimental animals were injected with either formalin ("PAIN" sampling group) or PBS ("CONTROL" sampling group). This change was done for clearer and stronger fluorescence results since the right amygdala has been observed to have greater activity during pain processing (Ji and Neugebauer, 2009; Allen et al., 2021; Miyazawa et al., 2018). This amygdala is also mostly responsible for pain modulation of the left side of the body (Cooper et al., 2018).

During the tonic/inflammation phase of the formalin test procedure, the von Frey filaments were utilized by briskly tapping their tips on the injection site, the skin in-between the paw pads. The filaments are graded according to increasing firmness, designated as G values. A higher G value will lend a stronger force when used as described. A mouse experiencing noxious tactile sensation will exhibit the paw withdrawal reflex. Thus, a mouse with pain-induced hyperalgesia was expected to perform the reflex when used with a comparatively softer filament.

An additional sampling group, designated as the "BASE" group, was included for comparison with the PAIN group. This group was injected with formalin in the same manner as described, but did not receive any tactile stimulation. The fluorescence

signals from the three sampling groups was the basis for interpreting the presence of hyperalgesia brain activity and was confirmed by the aesthesiometer G values that induced observed paw withdrawal reflex.

Imaging data was presented and qualitatively analyzed through three 15 x 15 pixel regions-of-interest (ROIs) per brain region. The basis for selection of the ROIs was how distinct the fluorescent forms are, meaning they have discernible outlines that can be discriminated. No further image data processing was done as of this moment.

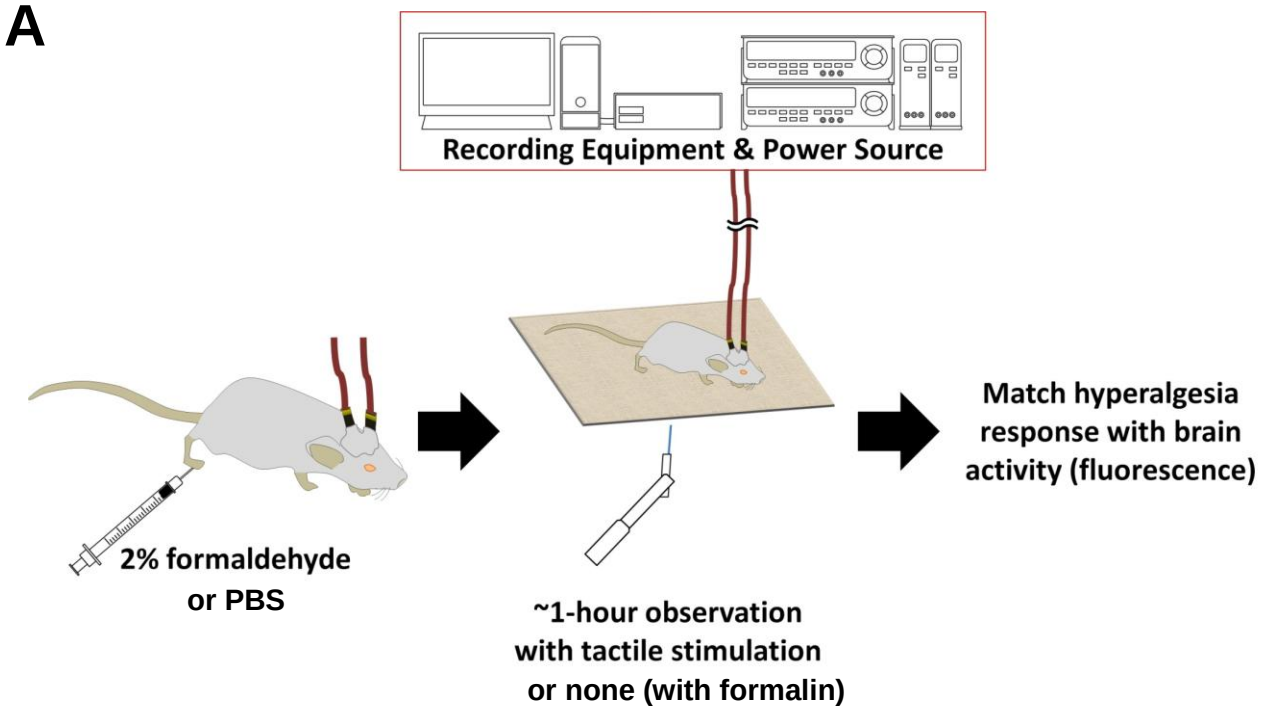

B

Figure 15. von Frey - Formalin test with brain activity imaging. (A) The experimental design of the von Frey - formalin hybrid test; this experiment involves three sampling groups, with two controls. (B) The actual von Frey filaments/aesthesiometers used, undeployed (left) and deployed (right).

b. Results

As of this moment, only qualitative data have been gathered and data processing has yet to be performed (**Fig. 16**).

The fluorescence signals in the Pain group are comparatively more intense, especially in the CeLC. The intensity is maintained after tactile stimulation. The signals in the DRN are also more consistently intense throughout the experiment proper, being more intense compared to the DRN ROIs of the other groups at around the last few minutes.

There is no apparent trend discerned form the data of the Control group, with the DRN or CeLC maintaining fluorescence intensity throughout the time span, depending on the replicate. The tactile stimulation has not resulted in any increase in or maintenance of fluorescence levels.

The bi-phasic pain response can be observed in the last two replicates of the Base group, more apparent in the CeLC of the former and the DRN of the latter. The fluorescence intensities of the CeLCs of the two aforementioned replicates are maintained throughout the experiment proper, but not of the DRNs.

The presence of hyperalgesia in the Pain group is corroborated by the observed withdrawal reflex induced by the 0.16G filament, except for one replicate. In contrast, all the mice of the Control group required the 1.0G filament to elicit the same response.

A

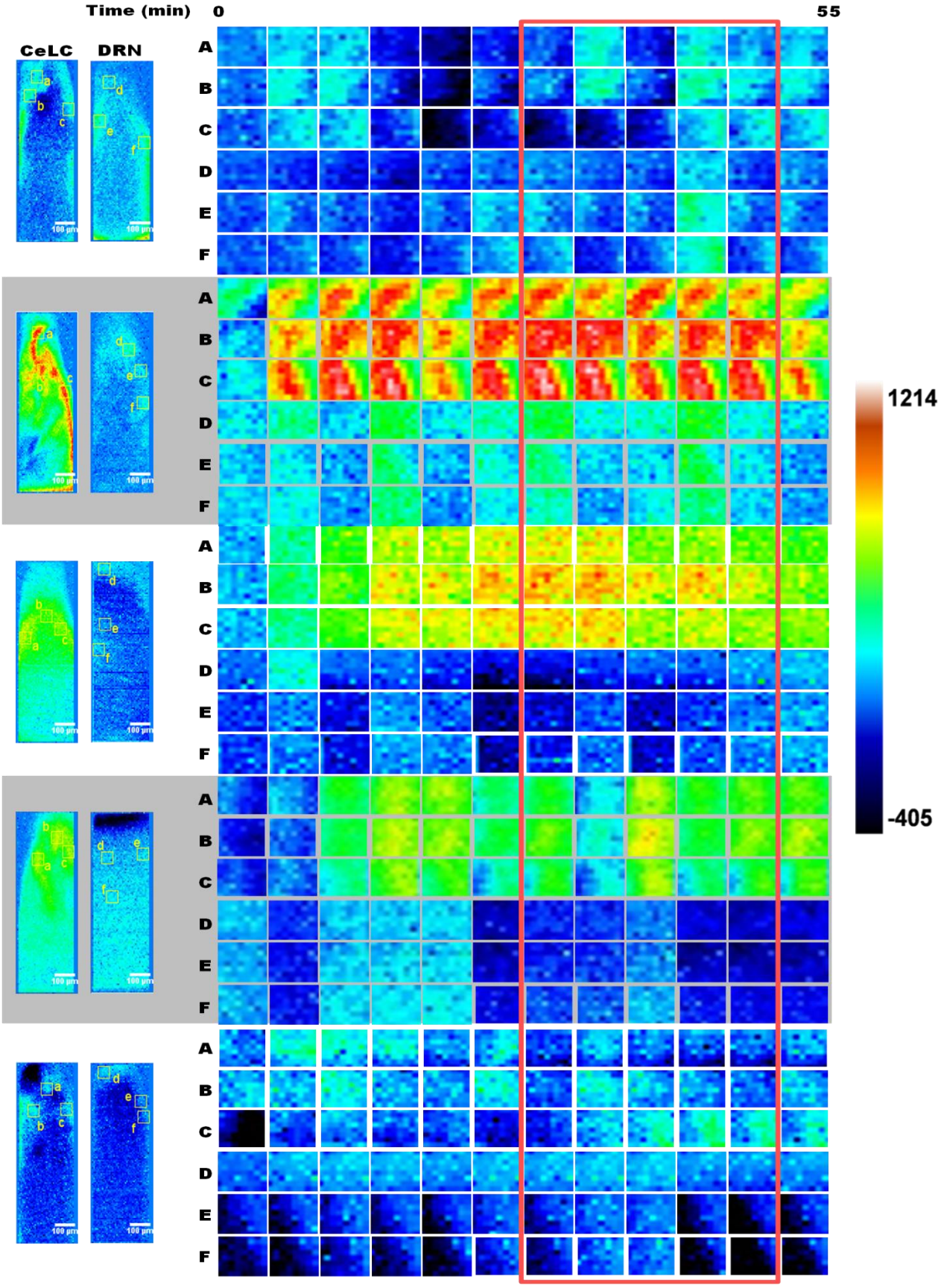

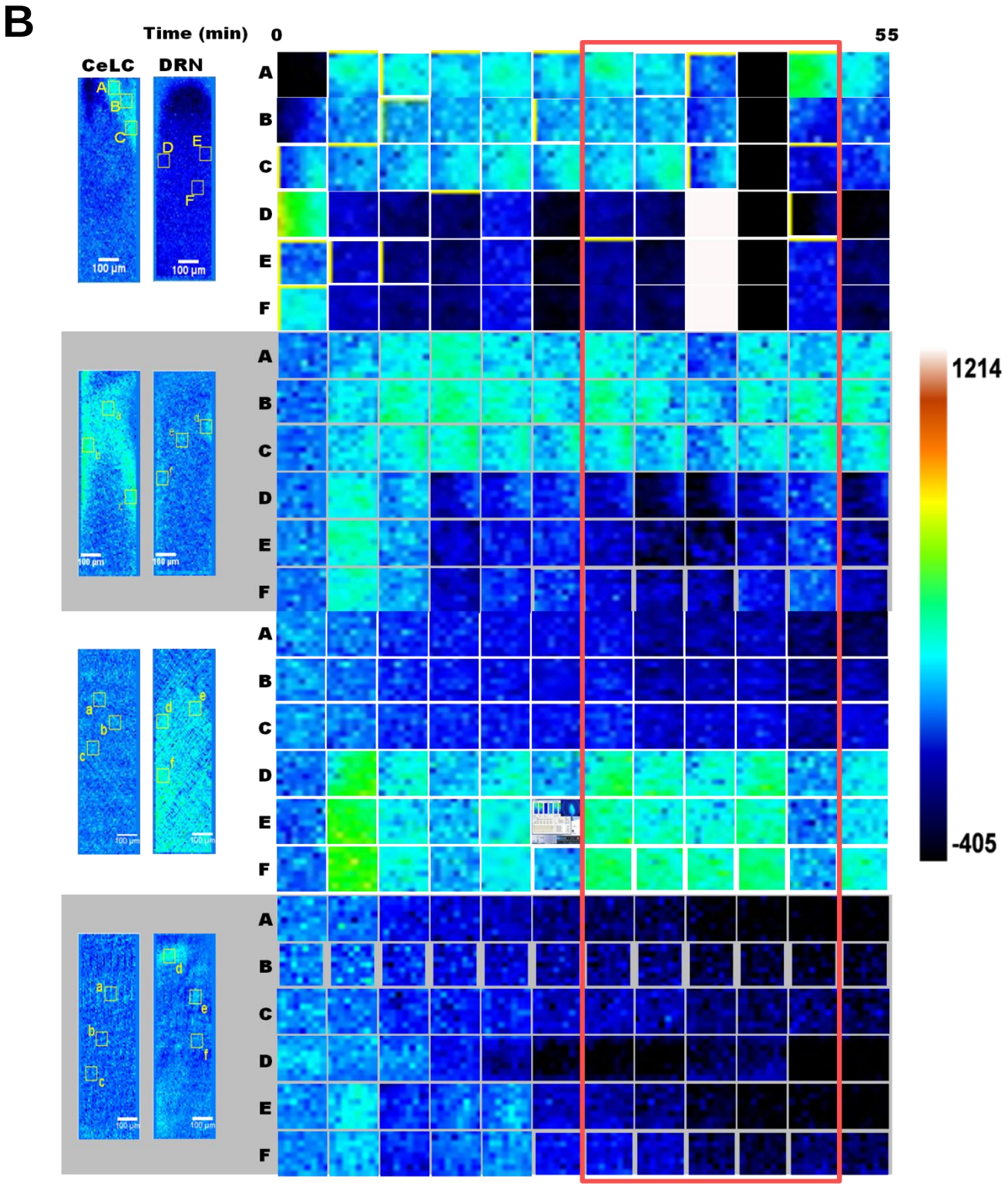
B
Time (min)
0
55
CeLC
DRN
A
B
C
D
E
F
100 µm
1214
-405

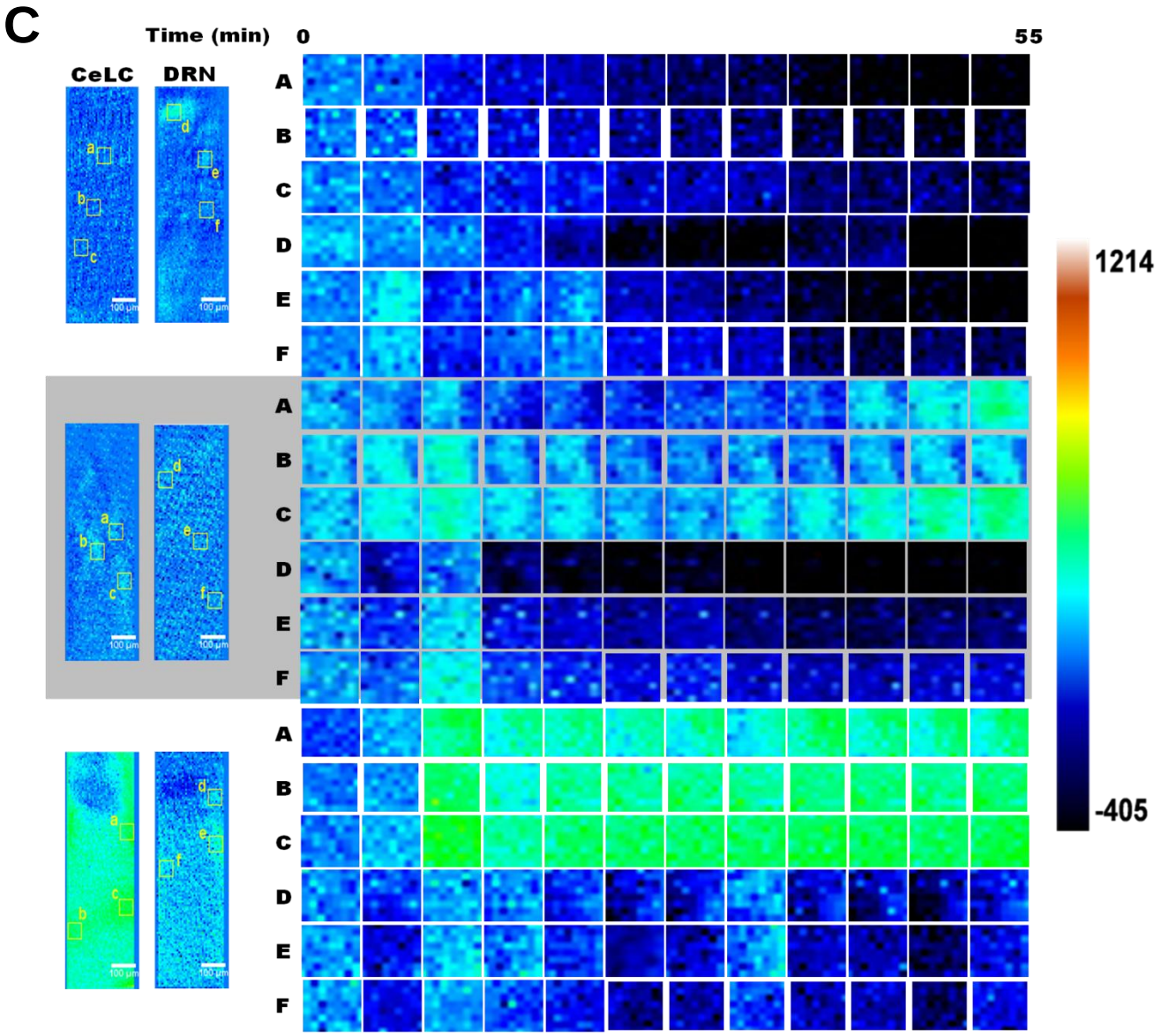

Figure 16. Fluorescence signals from ROIs of experimental animals. (A) ROIs of the Pain group (n=5), (B) of the Control group (n=4), and (C) of the Base group (n=3). Each square represents visual data sampling from the start of every 5 minutes. Rows **A** to **C** are from the CeLC and rows **D** to **F** are from the DRN. ROIs enclosed in the red boxes are from during tactile stimulation. Heatmap values are voltage values that represent ΔF.

c. Discussion

Calcium signalling fluorescence observed in the Pain group has shown that tactile stimulation can lead to persistent activation of the CeLC and the DRN in mice experiencing pain.

CeLC activity enhances pain sensation during inflammation (Veinante et al., 2013; Shinohara et al., 2017) that must have contributed to the observed persistent calcium signal. This enhancement is even not localized to the afflicted region (Sugimoto et al., 2021). Activation of amygdala can give rise to hyperalgesia (Dalmolin et al., 2007; Rouwette et al., 2012). Though, the CeLC is more responsible for the emotional dimension of pain sensation (Zhang et al., 2013). Stress itself can significantly contribute to the emergence of the inflammation through CeLC activation (DeBerry et al., 2015; Itoga et al., 2016). This might explain some of the long-lasting signals in the CeLC ROIs in some of the sample of the Control group since acute stress from the handling were present in all experimental animals, but the results suggest that is not as impactful as the effect of hyperalgesia itself.

The DRN activity is increased during inflammatory pain via the enhancement of the 5-HT (serotonin) signalling (Xie et al., 2002). This effect is immediate and can reach its peak in a few hours, but might persist for a day (Zhang et al., 2000).

The results of the Base group closely correspond to the data of the previous experiment, but further replication will be done for better representation.

Overall, calcium imaging signals derived from the right hemisphere central amygdala has been comparatively much more intense than from the other hemisphere

(see results from previous experiment). Imaging data from the Pain group have also shown stronger signals from the CeLC, as expected from its more prominent role in pain processing.

Further elucidation of the data will be done in the near future with appropriate data analysis. One of the goals is to quantify the presented image data to give a better resolution of the brain activity changes through time.

d. Summary

A combined von Frey – formalin test was done to expand upon the applications of the CMOS-based imaging devices. The goal of the experiment was to successfully acquire visual evidence of enhanced brain activity arising from hyperalgesia.

The procedure is very similar to the previously done formalin test but modified to accommodate the tactile stimulation needed to demonstrate hyperalgesia. During the later inflammation phase, the injected paws were stimulated with von Frey filaments of varying firmness. Another replication group was included without tactile stimulation. Visual data was presented as the changes of ROI fluorescence across the 1-hour span of the test.

The fluorescence data among the replication groups has shown that tactile stimulation with pain sensation relatively increased activation of the target brain sites, providing evidence of hyperalgesia.

6. Conclusion

a. Overview

We have shown that our developed implantable device can simultaneously be used to image two brain sites in mice while observing behavior, without hindrance or complications. The double implantation of the device was implemented across multiple experimental animals to successfully complete the modified formalin and the hybrid von Frey – formalin tests. The collected fluorescence imaging data has been useful to some degree, enough to show trends and support established findings about pain processing and hyperalgesia.

Modifications to the device and the peripheral equipment have enhanced efficiency of the utility of the device. It has been demonstrated that the established dual-imaging system, consisting of power sources, regulation boards, a recording computer, and connections, can operate in a sustained manner that allows for the successful experiment procedures. Improvement s done to the device cables and the FPC component of the needle-type device enhanced performance and ease-of-use. Lightening the overall cable weight permitted more mobility of the implanted mice and enhanced the lightweight feature of the devices. Strengthening the FPC rigidity reduced degree and frequency of the device warping and missing the target brain regions, though a balance between structure and berth had needed to be optimized.

Along with a more rigorous implantation and animal handling paradigm, experiments involving the imaging devices have proceeded with fewer impediments and complications. Strict and consistent implementation of the position levelling of the

bregma and lambda, landmarks found on the top skull surface, every implantation greatly improved accuracy of the targeting of small brain regions. This corresponds to the guidelines set by implantation protocols. Avoidance of critical brain regions, such as major blood vessels, essential brain sites, and ventricles, during implantation was also implemented by taking advantage of the device features that allows for angled implantations. By shifting the implantation trajectory, the least-injurious path was determined and followed, particularly for the DRN.

Application of the dual-imaging method for a slightly modified formalin test was successful. Calcium imaging data collected showed differences between mice experiencing pain and not. This is corroborated by time-matching and the Mutual Information determination with the observed pain-based behavior. More precise ROI analyses on another set of data demonstrated that the Formalin-injected group have brain regions synchronised in their activities, supporting the fact of their actual roles in pain processing. Temperature readings in the vicinity of implanted, activated devices have shown no signs of dangerous levels of heat. This supports the lack of indication of implanted mice distress and injury.

Lastly, the second implementation of the dual-imaging system in a hybrid von Frey – formalin test successfully visualized the brain activity during hyperalgesia. Primary qualitative calcium imaging of the CeLC and the DRN has shown sustained activity during tactile stimulation of mice experiencing formaldehyde-induced inflammation. This was in contrast to the lack of trends and lower signal intensity observed in the painless and tactile stimulation-less controls. Paw-withdrawal response with the softer tactile filaments in the majority of the Pain-group mice supports the

imaging data and the presence of hyperalgesia in said group. More replication for the control and non-tactile stimulated groups and formalized data processing and analyses will be done to make the data conclusive.

b. Future direction and possible applications

There much is a need for further device development, since at this point, the device is not sensitive enough to provide conclusive visuals. With the data alone, it is difficult to be conclusive about the actual identity of the fluorescent forms. What is certain is that the devices can reliably monitor and visualize brain activity in fluorescent transgenic mice. Proper selection of more active brain regions to image may better demonstrate its features and provide cleared images. The properties of this implantable CMOS device will make it easy to apply on novel sites and configurations in future experiments.

Because the protocols that were used, from the lens-less CMOS-based fluorescence imaging device usage to the general experimental design modifications, are quite novel, there are many points for improvement that need to be addressed. Long-term double-implantation use of the devices can be explored. The methodology used to demonstrate the device, the formalin test, is very short in duration. It did not allow for the exploration of this aspect of device use. Determining the long-term viability of an implanted device would expand applications to studies involving chronic pain or multi-stage pain-conditioning experiments involving the same experimental animals. Retention of dual-implantation for an extended period can also more ensure better and

much longer recuperation of the animals and give insight to potential changes to the integrity of the implanted devices. This can be feasibly done in future work because of the parylene coating, usually used on medical implants, that provides long-lasting bio-compatibility and protection from biological chemistry for implanted devices. Primary and unpublished data from previous attempts done in our lab have already proven this is most possible, but not to the extent of applying to actual long-term experimentation of double-implanted animals. The conditions of the animal and the target organ in a prolonged dual-implantation set-up are of greater uncertainty and can benefit more from further testing and investigation. This will require appropriate facilities that can house and shield the animal and the double-imaging system and modified equipment that can operate for a very long time.

The modular design of the device allows for components to be easily upgraded almost independent of each other. There are commercially-available CMOS imaging chips of superior performance that can potentially supplant what we have used, though it would take significant modification to make it compatible to the device design and objective. Such chips cannot be used in our imaging system as is. The imaging CMOS chips used by our devices were developed in-house for optimal use with the needle-type device. Size, imaging capacity, and heat-radiation levels were taken in to account to allow it to be used safely as part of a brain implant for calcium imaging. Adapting new CMOS-based imaging technology might require substantial development effort to make it feasible, and that will take time. Though, success can greatly improve the quality of the imaging data. Even so, image quality derived from the CMOS chips will almost always be of inferior quality compared to that from lens systems. Because of the optics

involved in a CMOS-based system versus a lens system, images from the former will never match the resolving power provided by the latter. Even with an increase in pixel amount, the resolution will not necessarily improve. What this study had provided is a starting point for possible use of better components to better approach data quality of already established tools, but also providing unique advantages. Materials for the FPC substrate can also be made thinner, but more rigid, to ensure better implantation accuracy and safety. The blue-light filter used on our CMOS chips has been developed in our lab (Sunaga et al., 2014) and is still being improved upon through integration of additional filtering layers and better fabrication methods. Thus, there is proof of concept that the dual use of the device can work, but the device has potential still for refinement.

Since the device has been developed more recently than other established inner-brain imaging devices, data processing methods for the collected visual data has not been well-established. Instead, adaptations of processing methods for visual data from the other devices are utilized that may not be wholly appropriate. Improper analysis might not properly bring the use of the device to its full potential. A more fitting method might be needed to be formulated to more properly process the new kind of data.

7. Bibliography

Allen, H. N., Bobnar, H. J., and Kolber, B. J. (2021). Left and right hemispheric lateralization of the amygdala in pain. *Progress in Neurobiology* 196, 101891. doi:10.1016/j.pneurobio.2020.101891.

Ammour, L., Heymes, J., Bautista, M., Fieux, S., Gensolen, F., Kachel, M., et al. (2019). MAPSSIC, a Novel CMOS Intracerebral Positrons Probe for Deep Brain Imaging in Awake and Freely Moving Rats: A Monte Carlo Study. *IEEE Trans. Radiat. Plasma Med. Sci.* 3, 302–314. doi:10.1109/TRPMS.2018.2881301.

Anderson, M., Zheng, Q., and Dong, X. (2018). Investigation of Pain Mechanisms by Calcium Imaging Approaches. *Neurosci. Bull.* 34, 194–199. doi:10.1007/s12264-017-0139-9.

Bernard, J. F., Peschanski, M., and Besson, J. M. (1989). A possible spino (trigemino)-ponto-amygdaloid pathway for pain. *Neuroscience Letters* 100, 83–88. doi:10.1016/0304-3940(89)90664-2.

Carrasquillo, Y., and Gereau, R. W. (2007). Activation of the Extracellular Signal-Regulated Kinase in the Amygdala Modulates Pain Perception. *Journal of Neuroscience* 27, 1543–1551. doi:10.1523/JNEUROSCI.3536-06.2007.

Cooper, A. H., Brightwell, J. J., Hedden, N. S., and Taylor, B. K. (2018). The left central nucleus of the amygdala contributes to mechanical allodynia and hyperalgesia following right-sided peripheral nerve injury. *Neuroscience Letters* 684, 187–192. doi:10.1016/j.neulet.2018.08.013.

Corder, G., Ahanonu, B., Grewe, B. F., Wang, D., Schnitzer, M. J., and Scherrer, G. (2019). An amygdalar neural ensemble that encodes the unpleasantness of pain. *Science* 363, 276–281. doi:10.1126/science.aap8586.

Cover, T. M., and Thomas, J. A. (2006). *Elements of information theory*. 2nd ed. Hoboken, N.J: Wiley-Interscience.

Cucchiaro, G., Chaijale, N., and Commons, K. G. (2005). The Dorsal Raphe Nucleus as a Site of Action of the Antinociceptive and Behavioral Effects of the α4 Nicotinic Receptor Agonist Epibatidine. *J Pharmacol Exp Ther* 313, 389–394. doi:10.1124/jpet.104.079368.

Dalmolin, G. D., Silva, C. R., Bellé, N. A. V., Rubin, M. A., Mello, C. F., Calixto, J. B., et al. (2007). Bradykinin into amygdala induces thermal hyperalgesia in rats. *Neuropeptides* 41, 263–270. doi:10.1016/j.npep.2006.12.007.

de Groot, A., van den Boom, B. J., van Genderen, R. M., Coppens, J., van Veldhuijzen, J., Bos, J., et al. (2020). NINscope, a versatile miniscope for multi-region circuit investigations. *eLife* 9, e49987. doi:10.7554/eLife.49987.

de Melo Reis, R. A., Freitas, H. R., and de Mello, F. G. (2020). Cell Calcium Imaging as a Reliable Method to Study Neuron–Glial Circuits. *Front. Neurosci.* 14, 569361. doi:10.3389/fnins.2020.569361.

DeBerry, J. J., Robbins, M. T., and Ness, T. J. (2015). The amygdala central nucleus is required for acute stress-induced bladder hyperalgesia in a rat visceral pain model. *Brain Research* 1606, 77–85. doi:10.1016/j.brainres.2015.01.008.

Finn, D. P., Chapman, V., Jhaveri, M. D., Samanta, S., Manders, T., Bowden, J., et al. (2003). The role of the central nucleus of the amygdala in nociception and aversion. *NeuroReport* 14, 981–984. doi:10.1097/01.wnr.0000069062.85441.29.

Flusberg, B. A., Cocker, E. D., Piyawattanametha, W., Jung, J. C., Cheung, E. L. M., and Schnitzer, M. J. (2005a). Fiber-optic fluorescence imaging. *Nat Methods* 2, 941–950. doi:10.1038/nmeth820.

Flusberg, B. A., Jung, J. C., Cocker, E. D., Anderson, E. P., and Schnitzer, M. J. (2005b). In vivo brain imaging using a portable 39?gram two-photon fluorescence microendoscope. *Opt. Lett.* 30, 2272. doi:10.1364/OL.30.002272.

Franklin, K. B. J., and Paxinos, G. (2008). *The mouse brain in stereotaxic coordinates*. Compact 3. ed. Amsterdam: Elsevier, Academic Press.

Franklin, K. B. J., and Paxinos, G. (2019). Paxinos and Franklin's the Mouse Brain in Stereotaxic Coordinates, Compact: The Coronal Plates and Diagrams.

Friedman, G. N., Grannan, B. L., Nahed, B. V., and Codd, P. J. (2015). Initial Experience with High-Definition Camera-On-a-Chip Flexible Endoscopy for Intraventricular Neurosurgery. *World Neurosurgery* 84, 2053–2058. doi:10.1016/j.wneu.2015.07.056.

Garcia-Garcia, A. L., and Soiza-Reilly, M. (2019). Serotonin Subsystems Modulate Diverse and Opposite Behavioral Functions. *ACS Chem. Neurosci.* 10, 3061–3063. doi:10.1021/acschemneuro.8b00534.

Gorissen, B., De Volder, M., and Reynaerts, D. (2018). Chip-on-tip endoscope incorporating a soft robotic pneumatic bending microactuator. *Biomed Microdevices* 20, 73. doi:10.1007/s10544-018-0317-1.

Grienberger, C., and Konnerth, A. (2012). Imaging Calcium in Neurons. *Neuron* 73, 862–885. doi:10.1016/j.neuron.2012.02.011.

Groessl, F., Munsch, T., Meis, S., Griessner, J., Kaczanowska, J., Pliota, P., et al. (2018). Dorsal tegmental dopamine neurons gate associative learning of fear. *Nat Neurosci* 21, 952–962. doi:10.1038/s41593-018-0174-5.

Han, J. S., and Neugebauer, V. (2004). Synaptic plasticity in the amygdala in a visceral pain model in rats. *Neuroscience Letters* 361, 254–257. doi:10.1016/j.neulet.2003.12.027.

Helmchen, F., Fee, M. S., Tank, D. W., and Denk, W. (2001). Two-Photon Microscope: High-Resolution Brain Imaging in Freely Moving Animals. 10.

Hunskaar, S., Fasmer, O. B., and Hole, K. (1985). Formalin test in mice, a useful technique for evaluating mild analgesics. *Journal of Neuroscience Methods* 14, 69–76. doi:10.1016/0165-0270(85)90116-5.

Hunskaar, S., and Hole, K. (1987). The formalin test in mice: dissociation between inflammatory and non-inflammatory pain. *Pain* 30, 103–114. doi:10.1016/0304-3959(87)90088-1.

Itoga, C. A., Roltsch Hellard, E. A., Whitaker, A. M., Lu, Y.-L., Schreiber, A. L., Baynes, B. B., et al. (2016). Traumatic Stress Promotes Hyperalgesia via Corticotropin-Releasing Factor-1 Receptor (CRFR1) Signaling in Central Amygdala. *Neuropsychopharmacol* 41, 2463–2472. doi:10.1038/npp.2016.44.

Jacob, A. D., Ramsaran, A. I., Mocle, A. J., Tran, L. M., Yan, C., Frankland, P. W., et al. (2018). A Compact Head-Mounted Endoscope for In Vivo Calcium Imaging in Freely Behaving Mice. *Current Protocols in Neuroscience* 84, e51. doi:https://doi.org/10.1002/cpns.51.

Ji, G., and Neugebauer, V. (2008). Pro- and Anti-Nociceptive Effects of Corticotropin-Releasing Factor (CRF) in Central Amygdala Neurons Are Mediated Through Different Receptors. *Journal of Neurophysiology* 99, 1201–1212. doi:10.1152/jn.01148.2007.

Ji, G., and Neugebauer, V. (2009). Hemispheric Lateralization of Pain Processing by Amygdala Neurons. *Journal of Neurophysiology* 102, 2253–2264. doi:10.1152/jn.00166.2009.

Ji, G., Zhang, W., Mahimainathan, L., Narasimhan, M., Kiritoshi, T., Fan, X., et al. (2017). 5-HT $_{2C}$ Receptor Knockdown in the Amygdala Inhibits Neuropathic-Pain-Related Plasticity and Behaviors. *J. Neurosci.* 37, 1378–1393. doi:10.1523/JNEUROSCI.2468-16.2016.

Kang, W., Wilson, M. A., Bender, M. A., Glorioso, J. C., and Wilson, S. P. (1998). Herpes virus-mediated preproenkephalin gene transfer to the amygdala is antinociceptive. *Brain Research* 792, 133–135. doi:10.1016/S0006-8993(98)00194-2.

Kim, Y. S., Anderson, M., Park, K., Zheng, Q., Agarwal, A., Gong, C., et al. (2016). Coupled Activation of Primary Sensory Neurons Contributes to Chronic Pain. *Neuron* 91, 1085–1096. doi:10.1016/j.neuron.2016.07.044.

Klioutchnikov, A., Wallace, D. J., Frosz, M. H., Zeltner, R., Sawinski, J., Pawlak, V., et al. (2020). Three-photon head-mounted microscope for imaging deep cortical layers in freely moving rats. *Nat Methods* 17, 509–513. doi:10.1038/s41592-020-0817-9.

Kraus, D. (2014). Consolidated data analysis and presentation using an open-source add-in for the Microsoft Excel® spreadsheet software. *Medical Writing* 23, 25–28. doi:10.1179/2047480613Z.000000000181.

Leblond, F., Davis, S. C., Valdés, P. A., and Pogue, B. W. (2010). Pre-clinical whole-body fluorescence imaging: Review of instruments, methods and applications. *Journal of Photochemistry and Photobiology B: Biology* 98, 77–94. doi:10.1016/j.jphotobiol.2009.11.007.

Lee, H. S., Eum, Y. J., Jo, S. M., and Waterhouse, B. D. (2007). Projection patterns from the amygdaloid nuclear complex to subdivisions of the dorsal raphe nucleus in the rat. *Brain Research* 1143, 116–125. doi:10.1016/j.brainres.2007.01.081.

Levene, M. J., Dombeck, D. A., Kasischke, K. A., Molloy, R. P., and Webb, W. W. (2004). In Vivo Multiphoton Microscopy of Deep Brain Tissue. *Journal of Neurophysiology* 91, 1908–1912. doi:10.1152/jn.01007.2003.

Li, W., and Neugebauer, V. (2004). Differential Roles of mGluR1 and mGluR5 in Brief and Prolonged Nociceptive Processing in Central Amygdala Neurons. *Journal of Neurophysiology* 91, 13–24. doi:10.1152/jn.00485.2003.

Li, Y., Wang, Y., Xuan, C., Li, Y., Piao, L., Li, J., et al. (2017). Role of the Lateral Habenula in Pain-Associated Depression. *Front. Behav. Neurosci.* 11. doi:10.3389/fnbeh.2017.00031.

Liberti, W. A., Perkins, L. N., Leman, D. P., and Gardner, T. J. (2017). An open source, wireless capable miniature microscope system. *J. Neural Eng.* 14, 045001. doi:10.1088/1741-2552/aa6806.

Lopes, P. S. S., Campos, A. C. P., Fonoff, E. T., Britto, L. R. G., and Pagano, R. L. (2019). Motor cortex and pain control: exploring the descending relay analgesic pathways and spinal nociceptive neurons in healthy conscious rats. *Behav Brain Funct* 15, 5. doi:10.1186/s12993-019-0156-0.

Lopez-Alvarez, V. M., Puigdomenech, M., Navarro, X., and Cobianchi, S. (2018). Monoaminergic descending pathways contribute to modulation of neuropathic pain by increasing-intensity treadmill exercise after peripheral nerve injury. *Experimental Neurology* 299, 42–55. doi:10.1016/j.expneurol.2017.10.007.

Mamede Rosa, M. L. N., Oliveira, M. A., Valente, R. B., Coimbra, N. C., and Prado, W. A. (1998). Pharmacological and neuroanatomical evidence for the involvement of the anterior pretectal nucleus in the antinociception induced by stimulation of the dorsal raphe nucleus in rats. *Pain* 74, 171–179. doi:10.1016/S0304-3959(97)00175-9.

Manning, B. H. (1998). A Lateralized Deficit in Morphine Antinociception after Unilateral Inactivation of the Central Amygdala. *J. Neurosci.* 18, 9453–9470. doi:10.1523/JNEUROSCI.18-22-09453.1998.

Manning, B. H., and Mayer, D. J. (1995a). The central nucleus of the amygdala contributes to the production of morphine antinociception in the formalin test. *PAIN*® 63, 141–152. doi:10.1016/0304-3959(95)00027-P.

Manning, B., and Mayer, D. (1995b). The central nucleus of the amygdala contributes to the production of morphine antinociception in the rat tail-flick test. *J. Neurosci.* 15, 8199–8213. doi:10.1523/JNEUROSCI.15-12-08199.1995.

Mehta, A. D., Jung, J. C., Flusberg, B. A., and Schnitzer, M. J. (2004). Fiber optic in vivo imaging in the mammalian nervous system. *Current Opinion in Neurobiology* 14, 617–628. doi:10.1016/j.conb.2004.08.017.

Mei, J., Riedel, N., Grittner, U., Endres, M., Banneke, S., and Emmrich, J. V. (2018). Body temperature measurement in mice during acute illness: implantable

temperature transponder versus surface infrared thermometry. *Sci Rep* 8, 3526. doi:10.1038/s41598-018-22020-6.

Miller, R. E., Kim, Y. S., Tran, P. B., Ishihara, S., Dong, X., Miller, R. J., et al. (2018). Visualization of Peripheral Neuron Sensitization in a Surgical Mouse Model of Osteoarthritis by In Vivo Calcium Imaging. *Arthritis & Rheumatology* 70, 88–97. doi:10.1002/art.40342.

Miyazawa, Y., Takahashi, Y., Watabe, A. M., and Kato, F. (2018). Predominant synaptic potentiation and activation in the right central amygdala are independent of bilateral parabrachial activation in the hemilateral trigeminal inflammatory pain model of rats. *Mol Pain* 14, 174480691880710. doi:10.1177/1744806918807102.

Neugebauer, V., and Li, W. (2002). Processing of Nociceptive Mechanical and Thermal Information in Central Amygdala Neurons With Knee-Joint Input. *Journal of Neurophysiology* 87, 103–112. doi:10.1152/jn.00264.2001.

Neugebauer, V., Li, W., Bird, G. C., and Han, J. S. (2004). The amygdala and persistent pain. *Neuroscientist* 10, 221–234. doi:10.1177/1073858403261077.

Oh, G., Chung, E., and Yun, S. H. (2013). Optical fibers for high-resolution in vivo microendoscopic fluorescence imaging. *Optical Fiber Technology* 19, 760–771. doi:10.1016/j.yofte.2013.07.008.

Ohkura, M., Sasaki, T., Sadakari, J., Gengyo-Ando, K., Kagawa-Nagamura, Y., Kobayashi, C., et al. (2012). Genetically Encoded Green Fluorescent Ca2+ Indicators with Improved Detectability for Neuronal Ca2+ Signals. *PLoS ONE* 7, e51286. doi:10.1371/journal.pone.0051286.

Ohta, J., Ohta, Y., Takehara, H., Noda, T., Sasagawa, K., Tokuda, T., et al. (2017). Implantable Microimaging Device for Observing Brain Activities of Rodents. *Proc. IEEE* 105, 158–166. doi:10.1109/JPROC.2016.2585585.

Ossipov, M. H., Dussor, G. O., and Porreca, F. (2010). Central modulation of pain. *J. Clin. Invest.* 120, 3779–3787. doi:10.1172/JCI43766.

Ozbay, B. N., Futia, G. L., Ma, M., Bright, V. M., Gopinath, J. T., Hughes, E. G., et al. (2018). Three dimensional two-photon brain imaging in freely moving mice using a miniature fiber coupled microscope with active axial-scanning. *Sci Rep* 8, 8108. doi:10.1038/s41598-018-26326-3.

Palazzo, E., Genovese, R., Mariani, L., Siniscalco, D., Marabese, I., de Novellis, V., et al. (2004). Metabotropic glutamate receptor 5 and dorsal raphe serotonin release

in inflammatory pain in rat. *European Journal of Pharmacology* 492, 169–176. doi:10.1016/j.ejphar.2004.03.063.

Peyron, C., Petit, J.-M., Rampon, C., Jouvet, M., and Luppi, P.-H. (1997). Forebrain afferents to the rat dorsal raphe nucleus demonstrated by retrograde and anterograde tracing methods. *Neuroscience* 82, 443–468. doi:10.1016/S0306-4522(97)00268-6.

Prakash, N., Stark, C. J., Keisler, M. N., Luo, L., Der-Avakian, A., and Dulcis, D. (2020). Serotonergic Plasticity in the Dorsal Raphe Nucleus Characterizes Susceptibility and Resilience to Anhedonia. *J. Neurosci.* 40, 569–584. doi:10.1523/JNEUROSCI.1802-19.2019.

Rao, J., Dragulescu-Andrasi, A., and Yao, H. (2007). Fluorescence imaging in vivo: recent advances. *Current Opinion in Biotechnology* 18, 17–25. doi:10.1016/j.copbio.2007.01.003.

Ren, J., Friedmann, D., Xiong, J., Liu, C. D., Ferguson, B. R., Weerakkody, T., et al. (2018). Anatomically Defined and Functionally Distinct Dorsal Raphe Serotonin Sub-systems. *Cell* 175, 472-487.e20. doi:10.1016/j.cell.2018.07.043.

Resendez, S. L., Jennings, J. H., Ung, R. L., Namboodiri, V. M. K., Zhou, Z. C., Otis, J. M., et al. (2016). Visualization of cortical, subcortical and deep brain neural circuit dynamics during naturalistic mammalian behavior with head-mounted microscopes and chronically implanted lenses. *Nat Protoc* 11, 566–597. doi:10.1038/nprot.2016.021.

Rosland, J. H. (1991). The formalin test in mice: the influence of ambient temperature. *Pain* 45, 211–216. doi:10.1016/0304-3959(91)90190-9.

Rosland, J. H., Tjølsen, A., Mæhle, B., and Hole, K. (1990). The formalin test in mice: effect of formalin concentration. *Pain* 42, 235–242. doi:10.1016/0304-3959(90)91167-H.

Ross, B. C. (2014). Mutual Information between Discrete and Continuous Data Sets. *PLoS ONE* 9, e87357. doi:10.1371/journal.pone.0087357.

Rouwette, T., Vanelderen, P., Roubos, E. W., Kozicz, T., and Vissers, K. (2012). The amygdala, a relay station for switching on and off pain: Role of limbic corticotropin-releasing factor in neuropathic pain. *EJP* 16, 782–792. doi:10.1002/j.1532-2149.2011.00071.x.

Rustami, E., Sasagawa, K., Sugie, K., Ohta, Y., Haruta, M., Noda, T., et al. (2020). Needle-Type Imager Sensor With Band-Pass Composite Emission Filter and Parallel Fiber-Coupled Laser Excitation. *IEEE Trans. Circuits Syst. I* 67, 1082–1091. doi:10.1109/TCSI.2019.2959592.

Sabetkasaei, M., Masoudnia, F., Khansefid, N., and Behzadi, G. (2007). Opioid Receptors of the Central Amygdala and Morphine-Induced Antinociception. *Iran. Biomed. J.*, 6.

Sarihi, A., Heshmatian, B., Pahlevani, P., Komaki, A., and Haghparast, A. (2015). Reversible Inactivation of the Dorsal Raphe Nucleus Increases Morphine-Induced Antinociception in Tolerated but Not in Nontolerated Rats. *Neurophysiology* 47, 205–211. doi:10.1007/s11062-015-9522-1.

Scott, B. B., Thiberge, S. Y., Guo, C., Tervo, D. G. R., Brody, C. D., Karpova, A. Y., et al. (2018). Imaging Cortical Dynamics in GCaMP Transgenic Rats with a Head-Mounted Widefield Macroscope. *Neuron* 100, 1045-1058.e5. doi:10.1016/j.neuron.2018.09.050.

Sela, Y., Hoekstra, M. M., and Franken, P. (2021). Sub-minute prediction of brain temperature based on sleep–wake state in the mouse. *eLife* 10, e62073. doi:10.7554/eLife.62073.

Shibata, M., Ohkubo, T., Takahashi, H., and Inoki, R. (1989). Modified formalin test: characteristic biphasic pain response. *Pain* 38, 347–352. doi:10.1016/0304-3959(89)90222-4.

Shinohara, K., Watabe, A. M., Nagase, M., Okutsu, Y., Takahashi, Y., Kurihara, H., et al. (2017). Essential role of endogenous calcitonin gene-related peptide in pain-associated plasticity in the central amygdala. *Eur J Neurosci* 46, 2149–2160. doi:10.1111/ejn.13662.

Silva, A. J. (2017). Miniaturized two-photon microscope: seeing clearer and deeper into the brain. *Light Sci Appl* 6, e17104–e17104. doi:10.1038/lsa.2017.104.

Spannuth, B. M., Hale, M. W., Evans, A. K., Lukkes, J. L., Campeau, S., and Lowry, C. A. (2011). Investigation of a central nucleus of the amygdala/dorsal raphe nucleus serotonergic circuit implicated in fear-potentiated startle. *Neuroscience* 179, 104–119. doi:10.1016/j.neuroscience.2011.01.042.

Sprouse, J. S., and Aghajanian, G. K. (1987). Electrophysiological responses of serotoninergic dorsal raphe neurons to 5-HT1A and 5-HT1B agonists. *Synapse* 1, 3–9. doi:10.1002/syn.890010103.

Stamford, J. A. (1995). Descending control of pain. *British Journal of Anaesthesia* 75, 217–227. doi:10.1093/bja/75.2.217.

Sugimoto, M., Takahashi, Y., Sugimura, Y. K., Tokunaga, R., Yajima, M., and Kato, F. (2021). Active role of the central amygdala in widespread mechanical sensitization in rats with facial inflammatory pain. *Pain* Publish Ahead of Print. doi:10.1097/j.pain.0000000000002224.

Sunaga, Y., Haruta, M., Takehara, H., Ohta, Y., Motoyama, M., Noda, T., et al. (2014). Implantable CMOS imaging device with absorption filters for green fluorescence imaging. in *Optical Techniques in Neurosurgery, Neurophotonics, and Optogenetics* (International Society for Optics and Photonics), 89280L. doi:10.1117/12.2038948.

Sunaga, Y., Ohta, Y., Akay, Y. M., Ohta, J., and Akay, M. (2020). Monitoring Neural Activities in the VTA in Response to Nicotine Intake Using a Novel Implantable Microimaging Device. *IEEE Access* 8, 68013–68020. doi:10.1109/ACCESS.2020.2985705.

Takehara, H., Katsuragi, Y., Ohta, Y., Motoyama, M., Takehara, H., Noda, T., et al. (2016). Implantable micro-optical semiconductor devices for optical theranostics in deep tissue. *Appl. Phys. Express* 9, 047001. doi:10.7567/APEX.9.047001.

Takehara, H., Ohta, Y., Motoyama, M., Haruta, M., Nagasaki, M., Takehara, H., et al. (2015). Intravital fluorescence imaging of mouse brain using implantable semiconductor devices and epi-illumination of biological tissue. *Biomed. Opt. Express* 6, 1553. doi:10.1364/BOE.6.001553.

Tappe-Theodor, A., and Kuner, R. (2019). A common ground for pain and depression. *Nature Neuroscience* 22, 1612–1614. doi:10.1038/s41593-019-0499-8.

Timme, N. M., and Lapish, C. (2018). A Tutorial for Information Theory in Neuroscience. *eNeuro* 5, ENEURO.0052-18.2018. doi:10.1523/ENEURO.0052-18.2018.

Tjølsen, A., Berge, O.-G., Hunskaar, S., Rosland, J. H., and Hole, K. (1992). The formalin test: an evaluation of the method. *Pain* 51, 5–17. doi:10.1016/0304-3959(92)90003-T.

Veinante, P., Yalcin, I., and Barrot, M. (2013). The amygdala between sensation and affect: a role in pain. *J Mol Psychiatry* 1, 9. doi:10.1186/2049-9256-1-9.

Wang, Q. P., and Nakai, Y. (1994). The dorsal raphe: an important nucleus in pain modulation. *Brain Res Bull* 34, 575–585. doi:10.1016/0361-9230(94)90143-0.

Wang, R. Y., and Aghajanian, G. K. (1982). Correlative firing patterns of serotonergic neurons in rat dorsal raphe nucleus. *J. Neurosci.* 2, 11–16. doi:10.1523/JNEUROSCI.02-01-00011.1982.

Wilson, T. D., Valdivia, S., Khan, A., Ahn, H.-S., Adke, A. P., Martinez Gonzalez, S., et al. (2019). Dual and Opposing Functions of the Central Amygdala in the Modulation of Pain. *Cell Reports* 29, 332-346.e5. doi:10.1016/j.celrep.2019.09.011.

Woolf, C. J. (2010). What is this thing called pain? *J. Clin. Invest.* 120, 3742–3744. doi:10.1172/JCI45178.

Xie, H., Ma, F., Zhang, Y.-Q., Gao, X., and Wu, G.-C. (2002). Expression of 5-HT2A receptor mRNA in some nuclei of brain stem enhanced in monoarthritic rats. *Brain Research* 954, 94–99. doi:10.1016/S0006-8993(02)03347-4.

Xiong, B., Li, A., Lou, Y., Chen, S., Long, B., Peng, J., et al. (2017). Precise Cerebral Vascular Atlas in Stereotaxic Coordinates of Whole Mouse Brain. *Front. Neuroanat.* 11, 128. doi:10.3389/fnana.2017.00128.

Xu, Q., and Dong, X. (2019). Calcium imaging approaches in investigation of pain mechanism in the spinal cord. *Experimental Neurology* 317, 129–132. doi:10.1016/j.expneurol.2019.03.002.

Yarmolenko, P. S., Moon, E. J., Landon, C., Manzoor, A., Hochman, D. W., Viglianti, B. L., et al. (2011). Thresholds for thermal damage to normal tissues: An update. *International Journal of Hyperthermia* 27, 320–343. doi:10.3109/02656736.2010.534527.

Yu, O., Parizel, N., Pain, L., Guignard, B., Eclancher, B., Mauss, Y., et al. (2007). Texture analysis of brain MRI evidences the amygdala activation by nociceptive stimuli under deep anesthesia in the propofol–formalin rat model. *Magnetic Resonance Imaging* 25, 144–146. doi:10.1016/j.mri.2006.09.022.

Zhang, R.-X., Zhang, M., Li, A., Pan, L., Berman, B. M., Ren, K., et al. (2013). DAMGO in the central amygdala alleviates the affective dimension of pain in a rat model of inflammatory hyperalgesia. *Neuroscience* 252, 359–366. doi:10.1016/j.neuroscience.2013.08.030.

Zhang, Y.-Q., Gao, X., Huang, Y.-L., and Wu, G.-C. (2000). Expression of 5-HT1A receptor mRNA in rat dorsal raphe nucleus and ventrolateral periaqueductal gray neurons after peripheral inflammation. *NeuroReport* 11, 3361–3365.

Zhou, W., Jin, Y., Meng, Q., Zhu, X., Bai, T., Tian, Y., et al. (2019). A neural circuit for comorbid depressive symptoms in chronic pain. *Nat Neurosci* 22, 1649–1658. doi:10.1038/s41593-019-0468-2.

Ziv, Y., and Ghosh, K. K. (2015). Miniature microscopes for large-scale imaging of neuronal activity in freely behaving rodents. *Current Opinion in Neurobiology* 32, 141–147. doi:10.1016/j.conb.2015.04.001.

8. Appendix

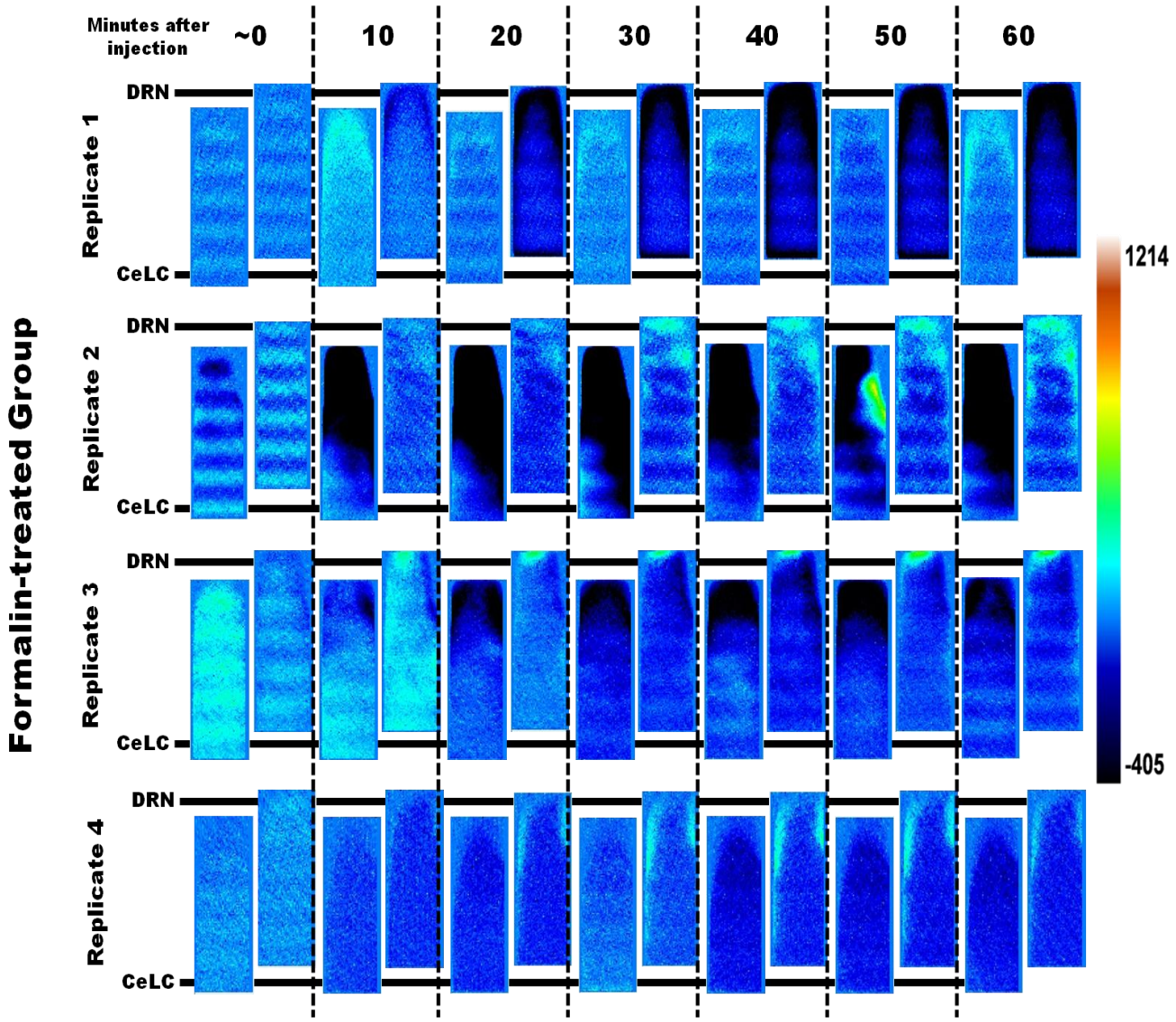
Minutes after injection
~0
10
20
30
40
50
60
Formalin-treated Group
Replicate 1
Replicate 2
Replicate 3
Replicate 4
DRN
CeLC
1214
-405

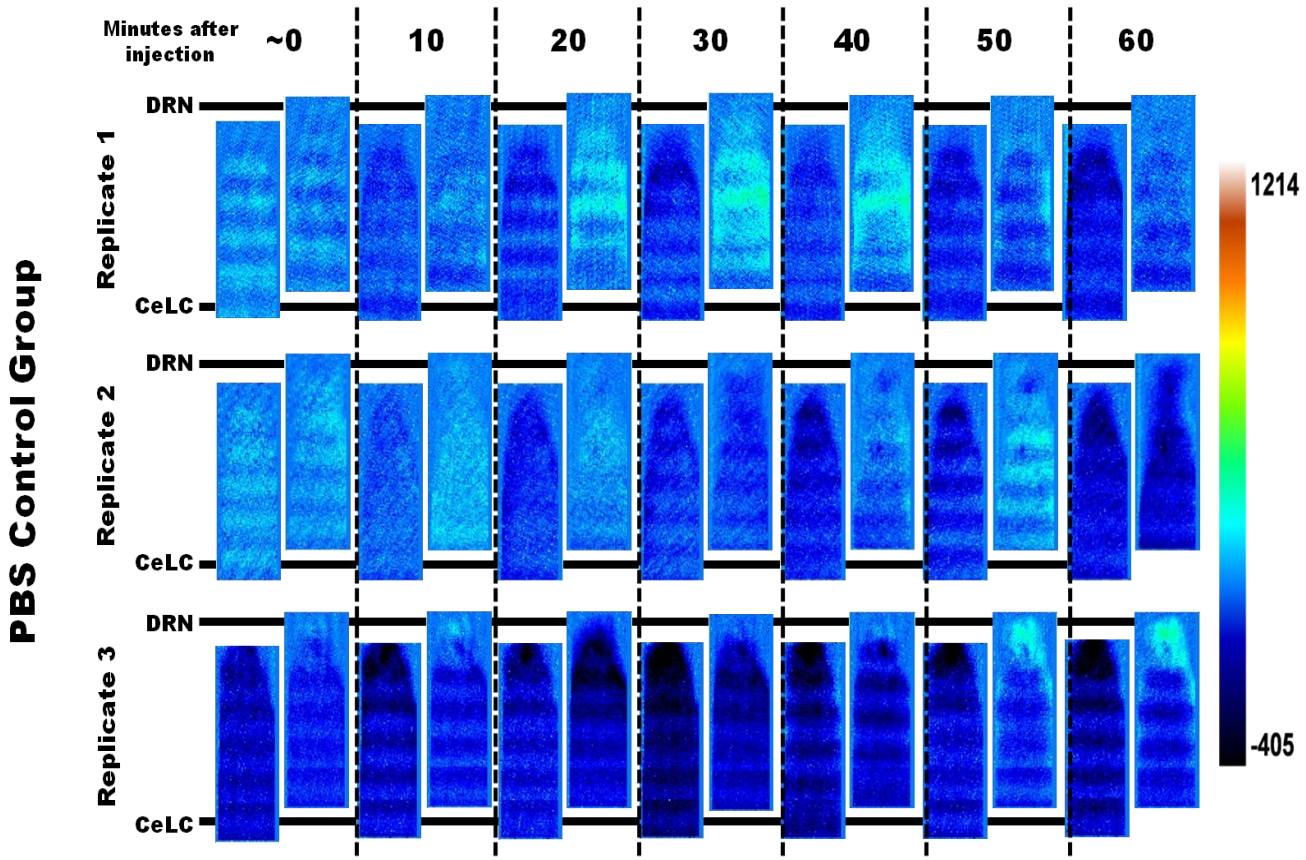

Appendix 1. Whole-frame calcium imaging of experimental animals implanted with devices containing TSM2020 imaging chips. Imaging data from formaldehyde-injected (n=4) and PBS-injected (n=3) GCaMP2 mice. The data is the basis for the Whole-frame Quantification and Averaging and Mutual Information Analysis with the time-matched behavior data. Heatmap values are voltage values that represent ΔF.

Amount of licks on the injected paw							
minutes	Formalin 1	Formalin 2	Formalin 3	Formalin 4	PBS Control 1	PBS Control 2	PBS Control 3
2.5	128	94	185	111	0	0	0
5	78	0	0	74	0	0	0
7.5	62	0	0	0	0	0	0
10	0	0	0	0	0	0	0
12.5	8	0	0	0	0	0	0
15	0	0	0	0	0	0	0
17.5	0	0	0	0	0	0	0
20	0	12	0	0	0	0	0
22.5	0	9	0	0	0	0	0
25	0	25	0	0	0	0	0
27.5	0	2	49	0	0	0	0
30	0	0	6	0	0	0	0
32.5	0	10	183	0	0	0	0
35	0	0	68	0	0	0	0
37.5	0	0	174	4	0	0	0
40	0	0	72	39	0	0	0
42.5	124	0	0	0	0	0	0
45	0	0	0	0	0	0	0
47.5	0	0	0	0	0	0	0
50	0	0	0	0	0	0	0
52.5	127	0	0	0	0	0	0
55	5	15	0	0	0	0	0
57.5	0	0	0	0	0	0	0
60	53	0	0	50	0	0	0

AVERAGE MI Coefficients				
	Formalin CeLC	Formalin DRN	PBS CeLC	PBS DRN
Mouse 1	0.128134569	0.109549913	1.11022E-16	1.11022E-16
Mouse 2	0.099800944	0.136143536	1.11022E-16	1.11022E-16
Mouse 3	0.10072687	0.092856499	1.11022E-16	1.11022E-16
Mouse 4	0.165736132	0.146986132		

Appendix 2. Tabulation of pain-related behavior (top) per time segment (2.5 mins) and the partially derived mutual information (MI) coefficients (bottom). Behavior tallied is strictly the licking of affected paw, until the experiment proper end.

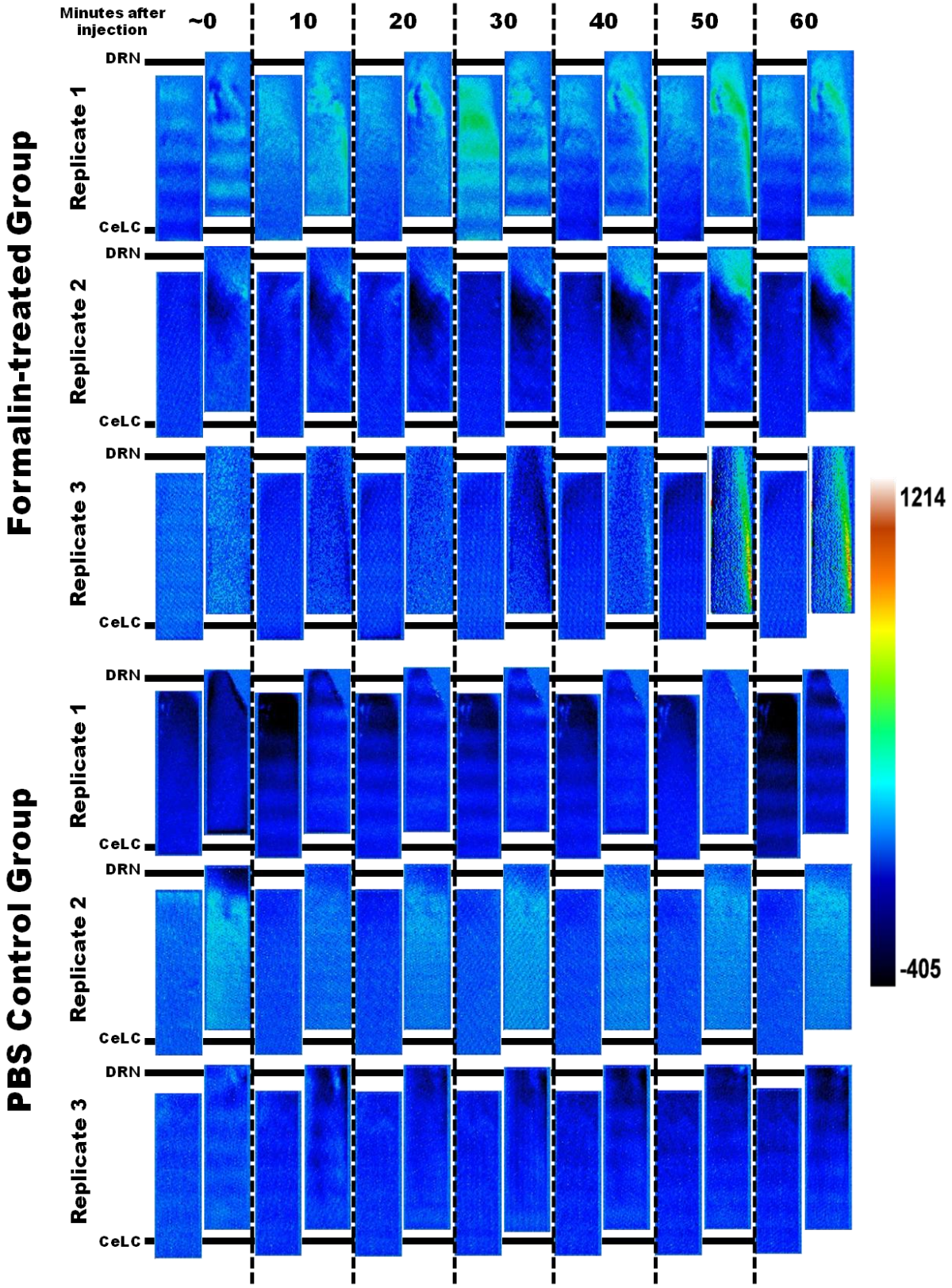
Minutes after injection
~0
10
20
30
40
50
60
Formalin-treated Group
PBS Control Group
Replicate 1
Replicate 2
Replicate 3
DRN
CeLC
1214
-405

Appendix 3. Whole-frame calcium imaging of experimental animals implanted with devices containing VIV imaging chips Imaging data from formaldehyde-injected (n=3) and PBS-injected (n=3) GCaMP2 mice. The data is the basis for the ROI Selection and Quantification and ROI Time-lag Cross Correlation Analyses. Heatmap values are voltage values that represent ΔF.

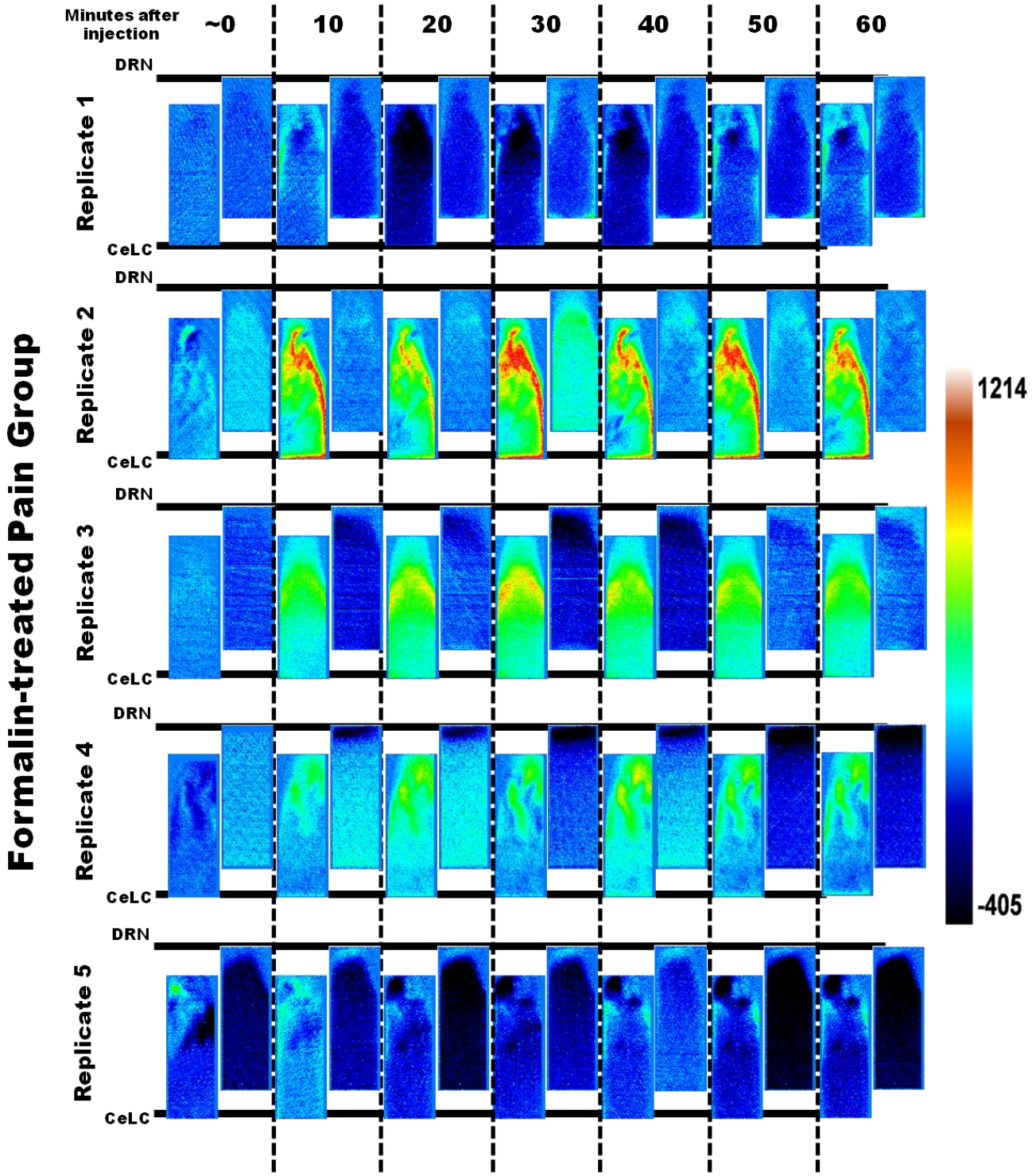
Formalin-treated Pain Group
Minutes after injection
~0
10
20
30
40
50
60
Replicate 1
Replicate 2
Replicate 3
Replicate 4
Replicate 5
DRN
CeLC
1214
-405

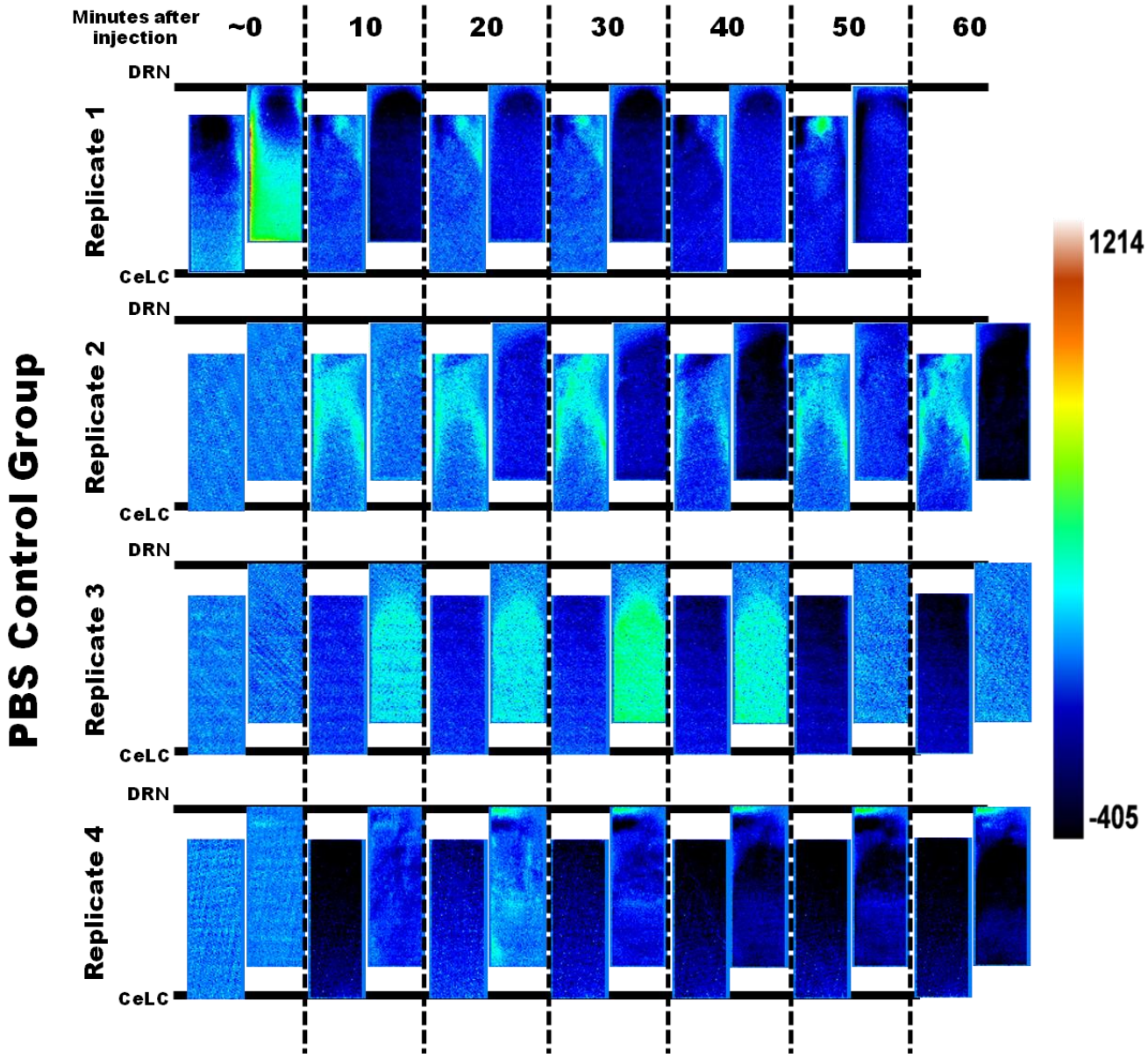
PBS Control Group
Minutes after injection
~0
10
20
30
40
50
60
Replicate 1
Replicate 2
Replicate 3
Replicate 4
DRN
CeLC
1214
-405

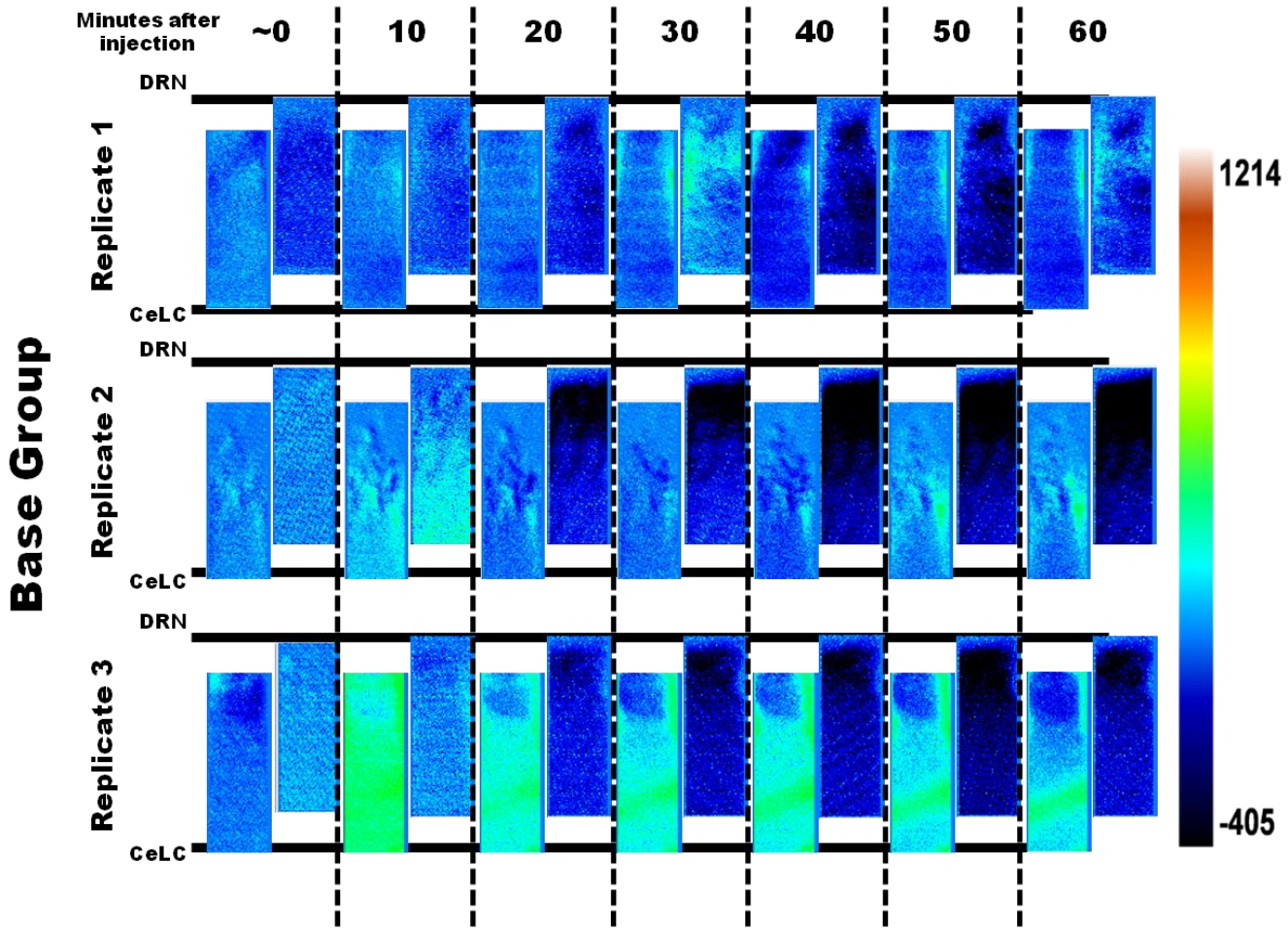

Appendix 4. Whole-frame calcium imaging of experimental animals included in the von Frey – formalin test Imaging data from formaldehyde-injected (Pain, n=5) and PBS-injected (Control, n=4) GCaMP6 mice that underwent tactile stimulation and formaldehyde-injected ones that did not (Base, n=3). The data is the source of the 15x15 px ROIs used in qualitative analysis. Heatmap values are voltage values that represent ΔF.